https://lib.uliege.be https://matheo.uliege.be

Master thesis and internship[BR]- Master's thesis : Study of the leading edge flow on compressor blades and the impact of incidence[BR]- Integration Internship

Auteur : Massaux, Nicolas
Promoteur(s) : Hillewaert, Koen
Faculté : Faculté des Sciences appliquées
Diplôme : Master en ingénieur civil en aérospatiale, à finalité spécialisée en "aerospace engineering"
Année académique : 2021-2022
URI/URL : http://hdl.handle.net/2268.2/16426

Avertissement à l'attention des usagers :

Tous les documents placés en accès ouvert sur le site le site MatheO sont protégés par le droit d'auteur. Conformément aux principes énoncés par la "Budapest Open Access Initiative"(BOAI, 2002), l'utilisateur du site peut lire, télécharger, copier, transmettre, imprimer, chercher ou faire un lien vers le texte intégral de ces documents, les disséquer pour les indexer, s'en servir de données pour un logiciel, ou s'en servir à toute autre fin légale (ou prévue par la réglementation relative au droit d'auteur). Toute utilisation du document à des fins commerciales est strictement interdite.

Par ailleurs, l'utilisateur s'engage à respecter les droits moraux de l'auteur, principalement le droit à l'intégrité de l'oeuvre et le droit de paternité et ce dans toute utilisation que l'utilisateur entreprend. Ainsi, à titre d'exemple, lorsqu'il reproduira un document par extrait ou dans son intégralité, l'utilisateur citera de manière complète les sources telles que mentionnées ci-dessus. Toute utilisation non explicitement autorisée ci-avant (telle que par exemple, la modification du document ou son résumé) nécessite l'autorisation préalable et expresse des auteurs ou de leurs ayants droit.

Master’s thesis submitted in order to obtain the master degree in
Aerospace Engineering

Study of the leading edge flow on compressor blades and the impact of incidence

---

Jury members:
Professor Koen HILLEWAERT (ULG)
Professor Vincent TERRAPON (ULG)
Professor Fabrizio FONTANETO (VKI)
Ir Loïc MARTIN (Safran)

Author:
Nicolas Massaux

Academic year: 2021-2022
University of Liège
Faculty of Applied Sciences - Civil engineering

Abstract

This work presents Direct Numerical simulations of a low pressure compressor cascade using a High order discontinuous Galerkin method. The High Performance Computing (HPC) massively parallel cluster, NIC5, made available by the University of Liège has made it possible to allocate a lot of resources in order to carry out the simulations. Four flow conditions are considered, which correspond to two solidities at two incidences. The flow velocity is at a Mach number of 0.45 for a corresponding Reynolds number of approximately 370 000. It is intended to understand the sudden rise of losses observed experimentally at a low solidity and a high incidence.

In general, the flow field is characterized by an extremely thick boundary layer on the suction side and a laminar flow on the pressure side. For the high incidence flow, the boundary layer reaches a thickness of 10% of the chord. All the flow conditions are subjected to Laminar separation bubble and turbulent flow reattachment near the leading edge. At high incidence and low solidity, the laminar separation bubble is very thick and short, the resulting boundary layer ends to separate at 60% of the chord.

Because the calculations were able to capture the complex physics of the flow. It was also able to predict the total pressure losses and flow angles, which showed a clear agreement with the experimental results.

Résumé

Ce travail présente des simulations numériques directes d'une cascade de compresseurs basse pression à l'aide d'un Galerkin discontinu d'ordre élevé. Le cluster massivement parallèle High Performance Computing (HPC), NIC5, mis à disposition par l'Université de Liège a permis d'allouer beaucoup de ressources afin de réaliser les simulations. Quatre conditions d'écoulement sont considérées, qui correspondent à deux solidités à deux incidences. La vitesse d'écoulement est à un nombre de Mach de 0,45 pour un nombre de Reynolds correspondant d'environ 370 000. Elle est destinée à comprendre la montée brutale des pertes observées expérimentalement à faible solidité et à forte incidence.

En général, le champ d'écoulement est caractérisé par une couche limite extrêmement épaisse sur la partie supérieure de l'aubage et un écoulement laminaire du côté inférieure. Pour l'écoulement à forte incidence, la couche limite atteint une épaisseur de 10% de la corde. Toutes les conditions d'écoulement sont soumises à une bulle de séparation laminaire et à un rattachement d'écoulement turbulent près du bord d'attaque. A haute incidence et faible solidité, la bulle de séparation laminaire est très épaisse et courte, la couche limite résultante finit par se séparer à 60% de la corde.

Parce que les simulations ont pu capturer la physique complexe de l'écoulement. Ils ont également été en mesure de prédire les pertes de charge totales et les angles d'écoulement, ce qui a montré un accord clair avec les résultats expérimentaux.

Acknowledgements

The completion of this master thesis would not have been possible without the help of many people.

Firstly, I would like to thank Professor Koen Hillewaert for its availability to answers to my questions, all its wise advice, all its feedbacks and, in a more general way, all the help that he gave to me even he was very busy.

I would also like to thank Ir. Margaux Boxho, which helped me in the setup of the probe grid and the computation of the velocity correlations in the boundary layer.

I would like to thank Ir. Nicolas Gianfolcaro for the help and advice he gave me during the elaboration of the thesis.

I would like to thank Professor Vincent Terrapon, Professor Fabrizio Fontaneto and Loïc Martin to serve on my jury.

Finally, I would like to thank Ir. Loïc Martin, working at Safran Aero Boosters, for mentoring me and providing me with the blading profile and experimental data.

Contents

List of Figures

List of Tables

Preamble

This thesis as part of a work of end of study aimed to carry out 4 numerical simulations, thanks to the resources made available by the university. Unfortunately, a few weeks before the submission of the thesis, one of the calculations stopped during the writing of the backup of the simulation. Unfortunately, this operation corrupted the save file. That'll teach me to make local backups of my work more regularly.

The case involved is the low-impact, high-solidity case (case). Due to the very good stability of the boundary layer, it is a calculation that takes a very long time to establish. This is why, the results which come from this case are not very faithful, and even for certain missing.

A lot of resources were allocated to recover this case, to the detriment of the three others. But at the end of the term, it became very difficult to allocate large amounts of resources.

1 Introduction

Reynolds-averaged Navier–Stokes (RANS) computations are the most well known and used method to solve complex turbulent flow. They require models, that in some cases, do not predict the correct physic of the flow. Safran Aero Boosters, in collaboration Von Karman Institute, carried out experimental test on a low pressure compressor cascade. It is designed to study the variation of the flow and loss mechanisms with respect to the solidity and incidence. For the low solidity cascade, a rapid increase of the losses at high incidence was measured. This phenomenon could not be captured using RANS simulations.

In order to understand the physics of the flow, Direct Navier-Stokes (DNS) simulations are carried on four different flow conditions. The computation are carried on NIC5, which is a cluster made available by the Université of Liège. The source code Argo has been provided by Professor Koen Hillewart (Uliège). Two solidities of $\sigma 1.1$ and 1.38 with two incidences $i = 6^{\circ}$ and $i = 8^{\circ}$ at Mach $M = 0.45$ are analyzed. It corresponds to a relatively low Reynolds number of $Re \approx 370,000$. The method features a 4th order accurate unstructured discontinuous Galerkin solver. Unlike, the RANS and the experimental results, the simulations are done without taking into account the effect of the end walls. A periodic domain, in the direction of the span, is considered.

The thesis is organized in three different sections. The first section explains all the methodology used to carry out the simulations. It briefly explains the numerical method being used. It details the boundary and initials conditions, how the computations were set up and how the meshing was done.

The second section is dedicated to certifying the good quality of numerical results. It is explained there how the time step is chosen and when to consider that a simulation has run long enough. Important parameters, such as the Mach number at the inlet, the mesh resolution and the velocity correlations around the blade are analyzed.

The last section provides an analysis of the results based on post-processing of the computed flows. The flow field is shown to illustrate different features such as transition and flow separation. Mach number and isentropic Mach number are analyzed. Finally, the numerical data are confronted to experimental one. Important quantities such as the total pressures losses and the flow angles are considered.

2 Methodology

This chapter describes the governing equations and the overall methodology adopted in the Direct Navier-Stokes (DNS) code, Argo, along with brief details on its implementation. Specific features of the code, such as temporal and spatial discretizations, boundary conditions, partitioning and parallelization are also explained in this section.

2.1 Numerical method

The equation that are being solved are Navier-Stokes equations (NSE). For compacity, NSE are written under a set of generic partial differential equations of convection-diffusion for the state vector $\tilde{u}$, composed of density, momentum and energy, defined on a domain Ω [7]

$$\frac{\partial \tilde{u}_m}{\partial t} + \nabla \cdot \mathbf{f}_m(\tilde{u}) + \nabla \cdot \mathbf{d}_m(\tilde{u}, \nabla \tilde{u}) = 0, \forall m. \tag{1}$$

Appropriate Dirichlet and Neumann boundary conditions are defined on the boundaries of the domain Ω. The index m represents the variable running from the state vector. $\mathbf{f}_m$ and $\mathbf{d}_m$ respectively represent the convective and diffusive fluxes. It is furthermore assumed that the diffusive fluxes **d** depend as follows on the solution and its gradients

$$\mathbf{d}_m^k = D_{mn}^{kl}(\tilde{u}) \frac{\partial \tilde{u}_n}{\partial x^l} \tag{2}$$

2.1.1 Spatial discretization

The DGM [5, 6, 7] is a Galerkin finite element method based on a “broken” interpolation space , composed of functions ϕ that are high-order polynomials on each of the elements e in the mesh, but not required to be continuous across the interfaces f between elements. Such an interpolation is illustrated in Fig. 1.

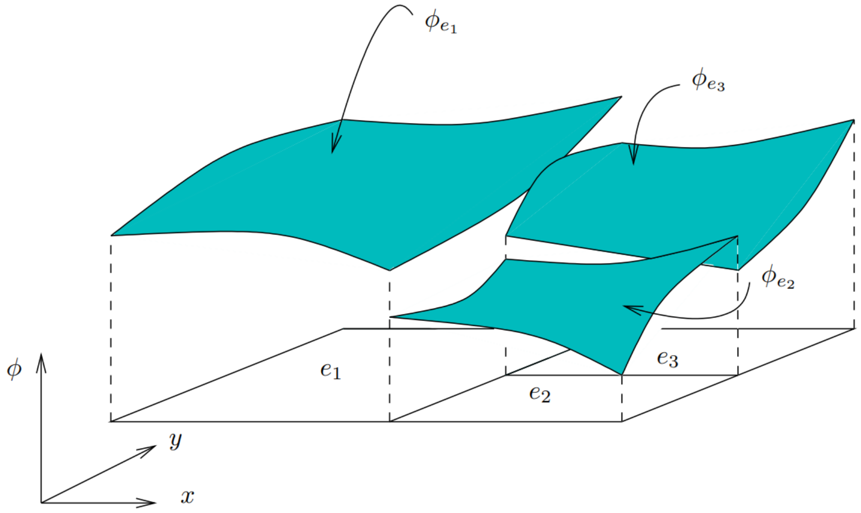

Figure 1: The discontinuous Galerkin interpolation space. [7]

After choosing an appropriate set of basis functions ϕ_i for $\Phi = \mathrm{span}\{\phi_1, \ldots, \phi_N\}$, with N the number of degrees of freedom per element, DGM then approximates the different components m of the solution state vector $\tilde{u}$ of u by

$$u_m = \sum_i \mathbf{u}_{im}\phi_i, \ \phi_i \in \Phi. \tag{3}$$

As for any Galerkin methods, the expansion weights $\mathbf{u}_{im}$ are found by requiring that the residual of the model equations, evaluated with u, is orthogonal to any function ϕ_i of the interpolation space Φ. This principle is further complemented with consistent terms at the element interfaces in order to ensure stability and convergence.

The method can easily be reinterpreted as composed of the combination of numerous Galerkin finite element problems, each defined on a single element, which are coupled by internal boundary conditions across the interfaces. For the convective terms, the Riemann solver assures the correct flux of characteristics that is emitted to and received from adjacent elements. It thus assures that the problem is correctly posed elementwise and also assures the global energy stability. In this paper, two different kinds of Riemann solver are being used. Classical ROE solver is used for both lower incidence simulations. While LAX FRIEDRICH Riemann solver is used for the two higher incidence simulations. This choice is enforced by the fact that at higher incidence, velocities in the laminar bubbles can be close or higher than speed of sound. When the laminar bubble turns turbulent, vortices that are ejected from the bubble can sometimes accelerate to reach very high Mach numbers. These very high speeds, which are concentrated only on a few elements, can cause divergence of the computation. LAX FRIEDRICH solver is more dissipative from a numerical point of view and thus prevent computation to reach infinite speed near leading edge. In this particular case, the solver is more stable but requires a smaller time step than the ROE one.

For the diffusive term, the symmetric interior penalty method is used. This method generalizes a boundary penalty method to enforce weak Dirichlet boundary conditions at the interfaces. More information about the penalty parameters, stability and general principles of the method can be found in [7].

In this thesis, the direct numerical simulations (DNS), of a turbulent flow through a low pressure compressor cascade, are carried out with a third order interpolation $p = 3$, which leads to a 4th order accurate discretization.

2.1.2 Temporal discretization

The time-integration scheme used for all the computation is an implicit two-point backward differentiation formula (BDF2) expressed as

$$\frac{df}{dt} \approx \frac{3f(t) - 4f(t - \Delta t) + f(t - 2\Delta t)}{2\Delta t}. \tag{4}$$

The BDF2 scheme is a method of choice in the computation of large-scale engineering flows [3]. It is linear multistep methods that, for a given function and time, approximate the derivative of that function using information from already computed time points, thereby increasing the accuracy of the approximation. It provides robustness, accuracy and stability while remaining fast. This discretization is preferred to others, such as ESKDIRK64 or other higher multistep methods. The latter being more precise, the compromise to be made in terms of precision and calculation time is not worth it.

The resulting non-linear implicit system of equations is solved using Newton-GMRES iterations. In the case of steady-state simulation, non-linear iterations are preconditioned by Incomplete LU (ILU). The resulting converged simulation is then used for unsteady computation, where non-linear iterations are preconditioned by block-Jacobi.

2.2 Computational domain and flow conditions

The blade to be studied has a chord c of 33 [mm]. The computational domain is a channel which is 4.5 times c. It is separated at the center of the blade profile, and the channel is raised to a height where it is centered with the trailing edge. The computational domain consists conceptually of a vertically infinite cascade, and it is extruded in the spanwise direction by 5% of c. The inlet of the domain is located one chord before the leading-edge (LE) while the outlet is located 2.5 chord after the trailing-edge (TE). The domain is taken long enough to destroy the large vortex structures generated during the transient phase, where the flow has to establish.

Computations are performed taking only one single blade into account. It receives homogeneous, undisturbed air, and there are no blade interactions downstream.

The vertical spacing (S) of the blades correspond to the height of the domain, which is

$$S = c/\sigma \tag{5}$$

where σ is the blade solidity. The cascade is operated at Mach = 0.45 with air at two different incidences for two different geometries. The four flow conditions that are used in this paper are resumed in Tab. 1, it's the combination of two solidities at two different incidences.

Mach [-]	**Incidence [°]**	**Blade Solidity [-]**
0.45	6	1.1
	8	1.38

Table 1: Table listing the four flow conditions that are being studied in this paper.

Finally, the stagger angle is $16.4°$ and the no-incidence angle is $32.4°$. The whole domain is depicted in Fig. 2.

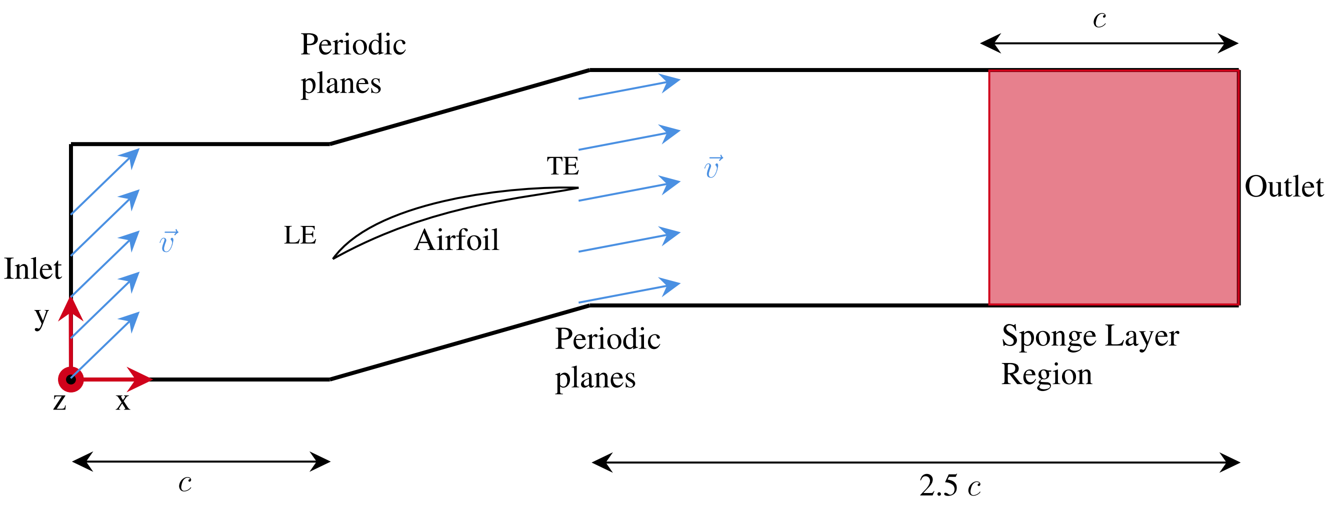

Figure 2: View of the computational domain from spanwise direction.

2.3 Boundary and initial conditions

A no-slip condition is put on the blade, and the wall is considered to be adiabatic.

A static pressure condition p_0 is put on the Outlet at a reference value of 101 325 Pascal.

A total condition is imposed on the inlet, where both total pressure p_1° and total temperature T_1° must be prescribed. The total temperature is computed as

$$T_1^\circ = T(1 + \frac{\gamma - 1}{2} M^2) = 305 \text{ [K]} \tag{6}$$

where $T = 293.15$ K is the reference temperature and γ the heat capacity ratio of air, which is 1.4. As a first approximation, the total pressure is computed as

$$p_1^\circ - \mathit{\Delta} p^\circ = p_0(1 + \frac{\gamma - 1}{2} M^2)^{\frac{\gamma}{\gamma - 1}} = 111900 \text{ [Pa]}. \tag{7}$$

The total pressure at the inlet must be adjusted for each simulation, it is done by increasing or decreasing the total pressure at the inlet. Indeed, using fixed pressure, the inlet Mach number decreases as losses in the cascade increases. Eq. 7 serves as a starting point to be in the right order of magnitude. At the end, $\mathit{\Delta} p^\circ \approx 1500$ [Pa] in order to reach the correct inlet Mach number. Moreover, the turbulent intensity at the inlet is zero, in order to let the turbulence settle naturally, the more the simulation advances.

Periodic boundary conditions are applied on periodic planes. It ensures the coupling between a pair of faces on either side of the blading. There are three pairs of faces in the vertical direction and 1 pair in the spanwise direction. Unlike the previous boundary conditions that are imposed in the software, periodicity is imposed at the mesh level. Faces on each coupled pairs must have the same topology, i.e. they must have collocated points such a one-to-one mapping exists between the faces on each side.

Finally, a Sponge layer of length c that covers the whole extrusion region is imposed near the outlet. It is a damping region, specified in volume of the computational domain, designed to remove flow fluctuations susceptible to cause spurious reflections at the outlet boundary. These unusual fluctuations are caused by the establishment of the boundary layer, and therefore a transient effect which is set to disappear. The damping is achieved by penalizing the difference between the local solution u and its (moving) time-average $\bar{u}$. The penalization method chosen is exponential. Zero everywhere (no penalization) and in the sponge layer it exponentially grows to reach infinity near the outlet (maximum penalization). An example of a computation that was performed without a sponge layer is shown in Fig. 3. The red circle shows anomalous turbulence that was created due to the establishment of the boundary layer. On the lower part of the image, we can see this turbulence is in $t_0 + \Delta t$. Without the Sponge layer, this turbulence moves towards the outlet without ever weakening and causes the simulation to stop.

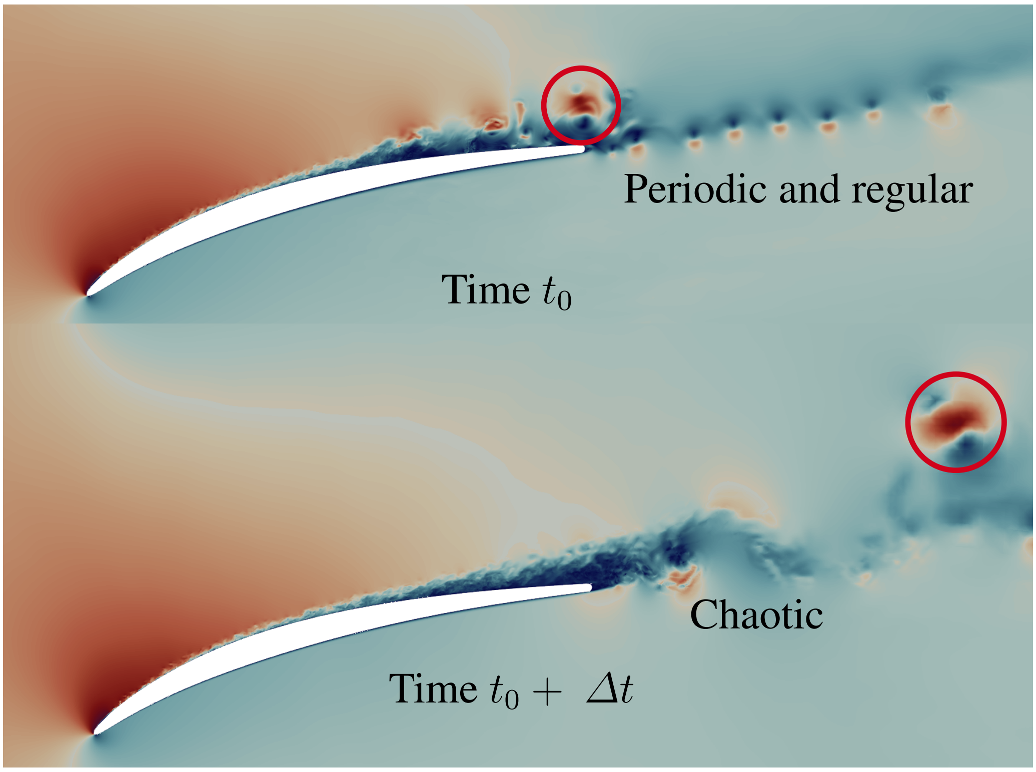

Figure 3: Example of the transient effects of a computation carried out without a sponge layer for two different time. The coloring shows the Mach number indicatively.

The initialization of the computation is realized in two distinct steps. A first steady-state simulation is carried out at order $p = 0$. The initial condition consists of imposing the total temperature at the inlet, the mach number and the flow angle. And to prescribe the same value everywhere in the domain.

The converged simulation is then used as an initial condition for the third order $p = 3$ unsteady computation. An example of such a computation shows the Mach field in Fig. 4. The zero order of the simulation can easily be seen on the mesh elements, where the calculated properties are constant across the cell. The advantage of this method is that it allows to align the flow according to the deflection caused by the blade. It also allows establishing a pseudo boundary layer. This "boundary layer" once the simulation is launched unsteady, will destabilize and give way to turbulence. Such a simulation takes a few minutes to converge. This therefore represents a huge time saving compared to a simulation that would be directly unsteady of order three.

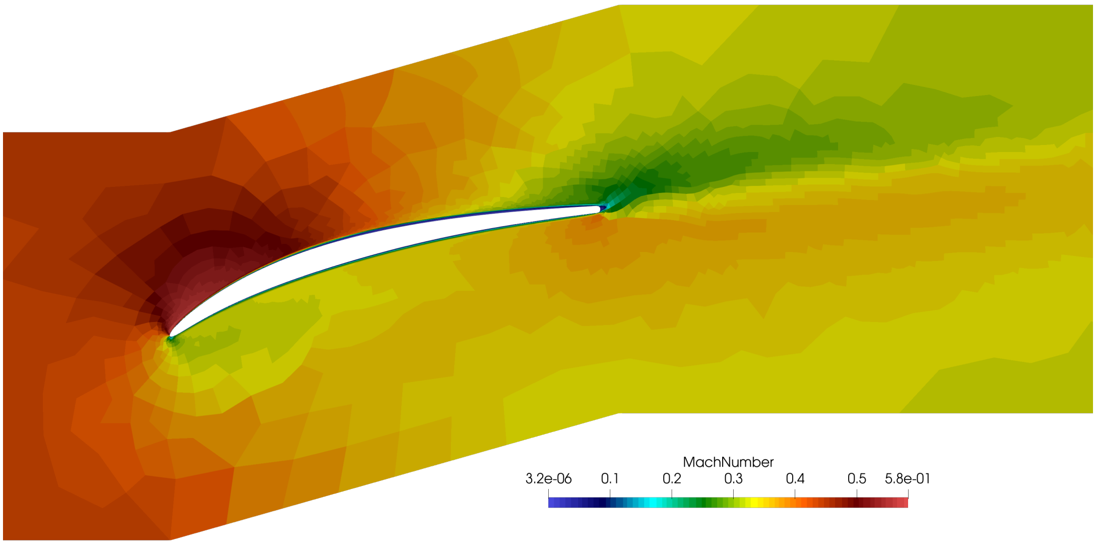

Figure 4: Converged steady-state simulation carried out of the 1.1 solidity cascade at 6° incidence.

2.4 Mesh description

The mesh used in the DGM computation is composed of only quad elements. The three-dimensional mesh is constructed by regular extrusion of a two-dimensional mesh specified on the periodic boundary.

The description of the geometry is carried out using curved mesh elements. Using quadratic polynomials, it results in a third-order accurate representation of the airfoil. Considering the high incidence of the flow, the mesh does not require the same level of precision everywhere on the geometry. To achieve fine mesh control on the geometry, the airfoil is represented using four different splines. In order to keep the quadratic continuity of the geometry, the junctions of the splines are made where the slope of the profile is as low as possible. The spline junctions are illustrated in red in Fig. 5. Because the mesh size can only be prescribed at the beginning or the end of the spline, it highlights four regions of interest, where the mesh can be finely controlled around the airfoil. These regions are, the trailing-edge, the region where the transition from laminar to turbulent occurs, the pressure side with trailing-edge and finally the pressure side.

The mesh size is prescribed in the leading edge and in the transition region to be constant. It is chosen to be a bit bigger on the suction side, and coarser on the pressure side, which require less resolution than previous regions. Between the region boundaries, the mesh size gradually adapts between to avoid sudden change in size.

In order to resolve the thin boundary layers along the no-slip boundary, a 2D boundary layer mesh is generated in the periodic plane. The first mesh element is prescribed both in

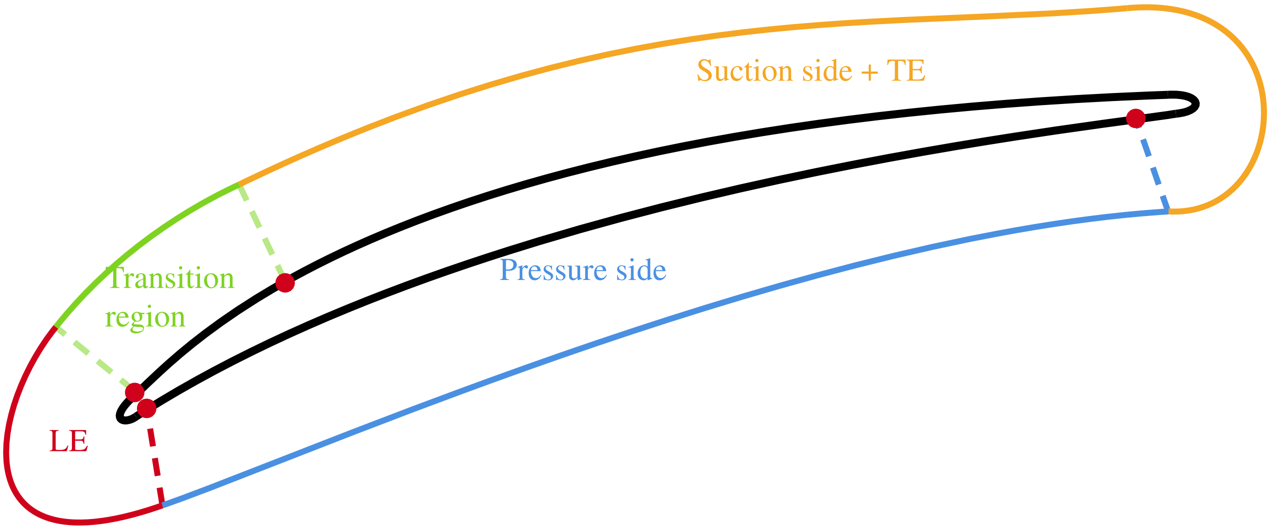

Figure 5: Representation of the geometry with mesh control points and different region of interest where the mesh can be fine-tuned.

height and width. The boundary layer mesh consists of 10 layers of homogeneous quad elements normal to the surface. The height of the following elements in this direction are determined using Beta Law with a beta coefficient of $\beta = 0.05$. Beta Law is more suitable for boundary layer mesh than regular geometric progression. It allows to significantly reduce the number of element while catching the high velocity gradient near the surface. Compared to regular progression, Beta Law has the same mesh density near the surface, however, a little higher, where the velocity gradients are less important, the meshes are larger. The effect of the beta law on the boundary layer is shown in Fig. 6. Using the same mesh size and by prescribing the length of the boundary layer, Beta Law leads to a decrease of nearly 40% of the total number of elements.

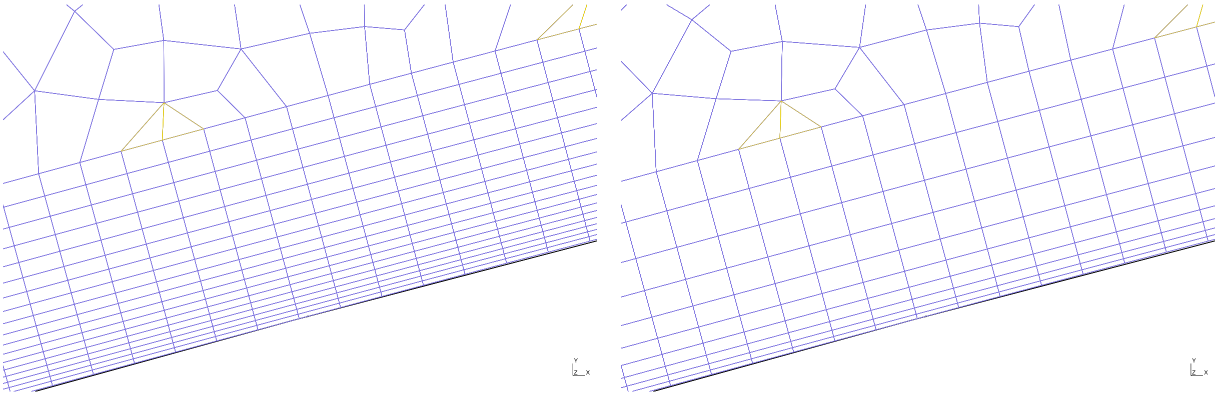

(a) Without Beta Law

(b) With Beta Law

Figure 6: Comparison of the Boundary Layer mesh with and without Beta Law.

The leading-edge (LE) and trailing-edge (TE) are two regions of interest where the curvature of the airfoil can be large. Decreasing the mesh size to have a good representation of the curvature leads to an over-refinement of the boundary. To prevent such a behavior and reduce the number of elements in the mesh, the mesh is adapted with respect to the curvature of the model at the LE and TE. It also avoids large mesh elements at the edge of the boundary layer. The value giving the target number of elements is fixed to 40 per 2π radians. The effect of mesh from curvature (MFC) adaption is illustrated in Fig. 7 and Fig. 8.

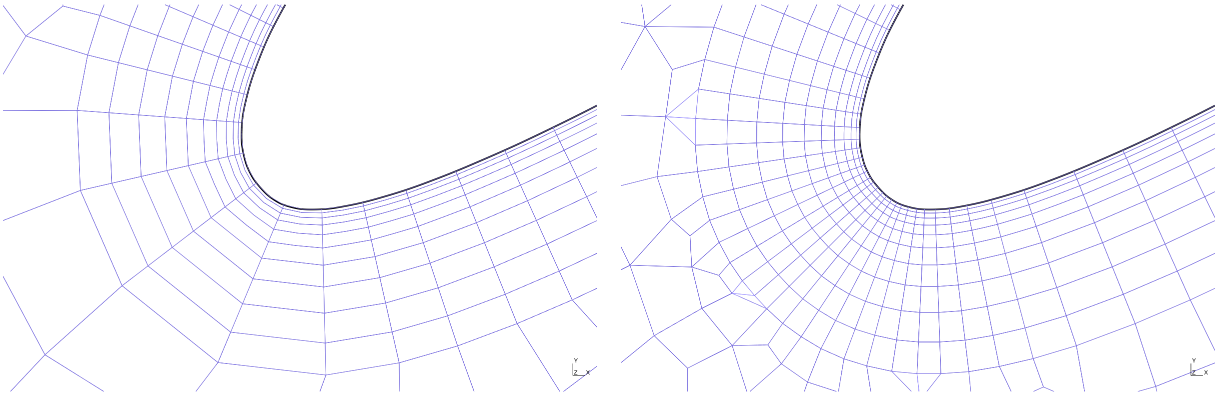

(a) Without MFC

(b) With MFC

Figure 7: Comparison of the mesh at leading edge with and without Mesh From Curvature (MFC) adaptation.

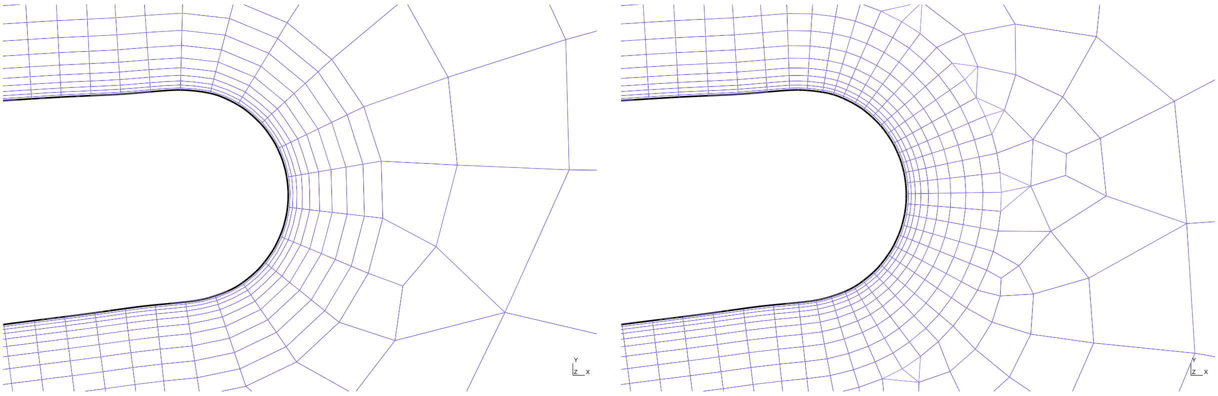

(a) Without MFC

(b) With MFC

Figure 8: Comparison of the mesh at trailing edge with and without Mesh From Curvature (MFC) adaptation.

The grid specifications are determined a posteriori during a number of preliminary two-dimensional runs in order to obtain sufficient resolution near critical regions (which are represented in red, green and orange in Fig. 5). The grid resolution is discussed in the Sec 3.4.

Extrusion mesh size is chosen such that the mesh is nearly isotropic at mid-chord of the suction side. In practice, it is difficult for this criterion to be respected everywhere along the airfoil surface. The leading-edge and transition region requires a chord-wise mesh resolution much smaller than the pressure or suction side region. The mesh isotropy is therefore reduced in favor of a more efficient distribution of the elements. It helps to reduce total number of elements and prevents the simulation to be over-resolved in some areas in the boundary layer. The surface mesh is shown in Fig. 9 for three stations.

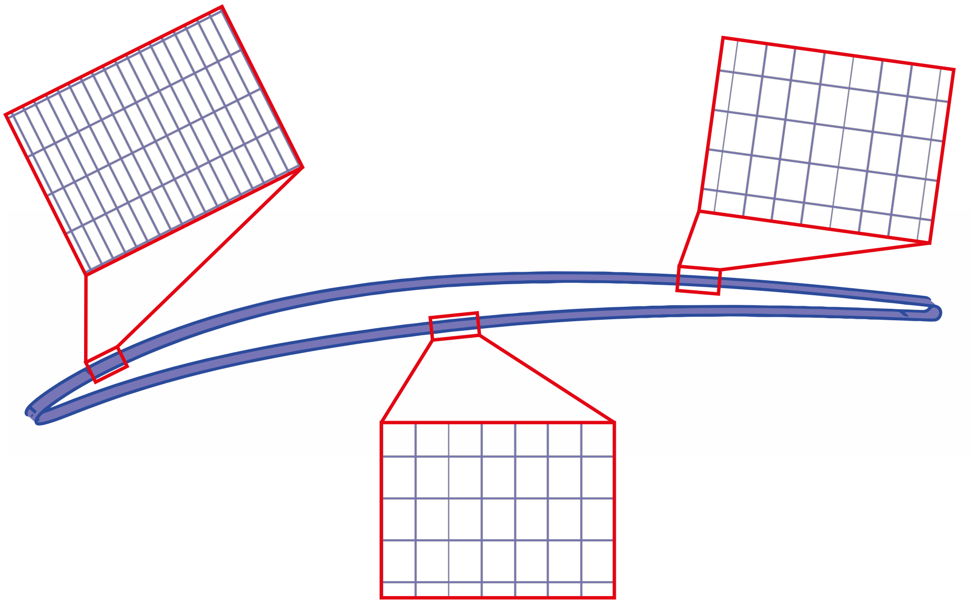

Figure 9: Side view of the airfoil surface with a view of the mesh at different stations.

Finally, the rest of the mesh is complemented with refinement inside the wake region. The refinement is one chord long after the trailing-edge. It is intended to correctly capture the wake, and to assess as accurately as possible the losses in the system.

Near the outer wall, the mesh size is much larger. Indeed, before reaching the blade, the flow is homogeneous, and therefore does not require a high mesh density. In the wake, the mesh is very fine and then coarsen approaching the outlet of the domain. This has two important effects, the first is to reduce the number of mesh elements. The second, in the case of the outlet, is to help the Sponge Layer breaks up large vortex structures. The establishment of the flow and the boundary layer around the airfoil is a favorable moment for the generation of such structures. These structures have nothing physical and are only due to the transitional phase. These vortex structures have a low pressure zone in their center. If one of these structures reaches the outlet, the pressure gradient between the center and the outlet can create very high local velocities entering or leaving the domain. These sudden high speeds can therefore lead to simulations to stop and never restart due to an impossibility to converge. Getting rid of these structures, during the transition phase, can be a real challenge. If they remain until it reaches the end of the domain, it means that the domain is too short, or that the mesh coarsening is not important enough. These phenomena are particularly strong for the case at 8° of incidence and a solidity of $\sigma = 1.1$.

An overall representation of the final mesh is shown in Fig. 10. Three zooms show zones of interest which are respectively the leading-edge, the trailing-edge and the wake. The final 3D meshes are constructed by extrusion of a 2D unstructured quadrilateral mesh in the spanwise direction (which corresponds to the direction z in Fig. 2). Such a mesh has between 288k and

300k elements, depending on the blade solidity.

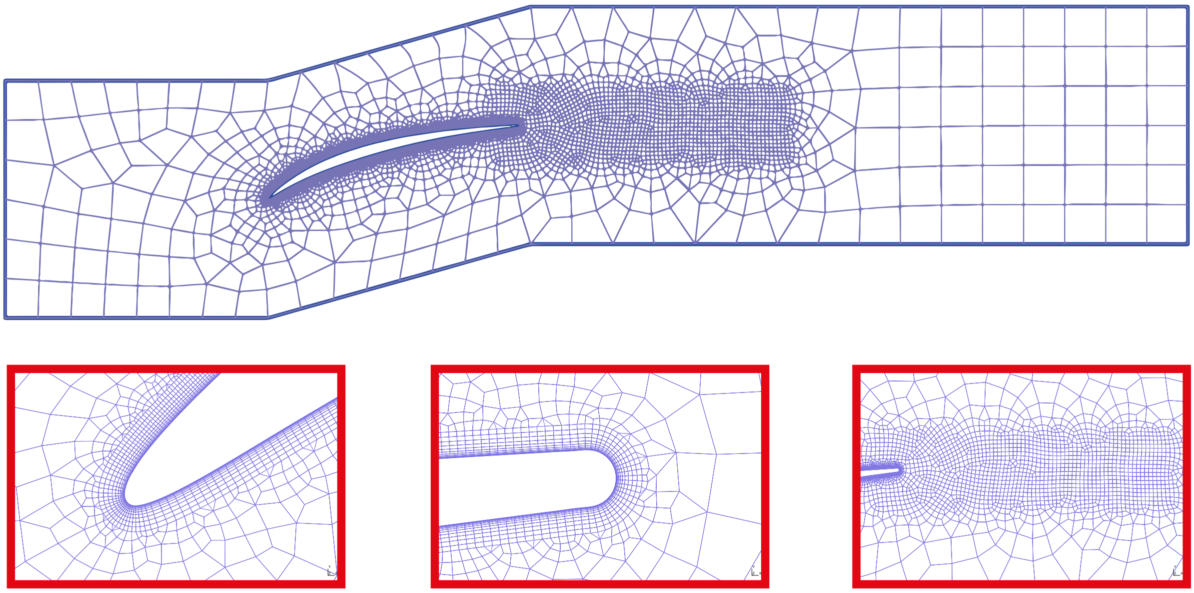

Figure 10: Representation of the final 2D mesh, used in the case of 1.1 solidity, on the periodic face.

2.5 Parallelization

Direct numerical simulation involves the direct solution of the NS equations. They are capable of resolving the smallest space and time scales of turbulence within a flow. Unlike a RANS method, DNS does not require any closure model. It is therefore necessary to use a very fine mesh and small time steps to obtain accurate solutions. On a regular computer, RANS can take up from few minutes to several hours, depending on the flow and the geometry complexity. On the other hand, DNS can take up from few days to weeks of computation.

To overcome this problematic, and obtain results over time for a graduation project, computations are accelerated thanks to high-performance computer equipment made available by Consortium des Équipements de Calcul Intensif (CÉCi). The main cluster being used is NIC5 [1], which is hosted at the University of Liège. It allows users to allocate a maximum of 320 processors to run parallel jobs.

In order to be more efficient, the mesh, as presented in Section 2.4, cannot be used in one chunk. It is partitioned into much smaller chunks, which are then each assigned to a processor to be simulated in parallel with the others. Data are then saved chunk by chunk, and therefore need to be recombined during post-processing. As a rule of thumb, one processor is assigned to approximately 1000 elements, which at order three wouldn't use more than 2 GB of ram per processor.

3 Results validation

In this section, information on the quality of the results is provided. The time step as well as the CFL (Courant-Friedrichs-Lewy) numbers are explained on each case, as well as the methodology used in the use of this one. Then, it is explained how a simulation is considered as converged in the unsteady sense. And from when the sampling for the time average starts. Mach number accuracy at the inlet is also provided. The mesh resolution is discussed as a function of the non-dimensional parameters of distance to and on the wall. Finally, a study of the correlation of speeds around the blading, makes it possible to quantify the distance of extrusion chosen between the two periodic planes

3.1 Time-step strategy

The time step used is a fixed time step strategy. Computations are restarted from the steady solution using a CFL number of 1, which is defined as

$$\text{CFL} = \frac{U \varDelta t}{\varDelta h} \tag{8}$$

Where U is the inlet flow velocity, $\varDelta t$ is the time step of the simulation and $\varDelta h$ is the characteristic size of the smallest mesh element.

As the simulation runs and turbulence sets in, the GMRES-Newton solver begins to converge slower and slower i.e. it requires more iteration for the non-linear solver to converge. At this moment, a compromise can be made, it could be judicious to decrease the time step. Halving the time step can sometimes lead to convergence of the time step more than two times faster. In this case, even if the time step is smaller, it represents a gain in terms of computation time. If this is not the case, the simulation will have gained in precision to the detriment of the calculation time, which will be longer. As the turbulent structures becomes smaller and smaller, there inevitably comes a time when the solver no longer converges. In general, a reduction of the time step by a factor of 2 makes it possible to solve this problem. In the case of high incidence simulations, this reduction in the time step also had to be accompanied by a change in the Riemann solver.

For every case, the time step at the beginning and at the end of the simulations are listed in Tab. 2.

Cases		**Beginning**		**End**	
Solidity σ [-]	**Incidence [°]**	**Time step $*1e^{-8}$ [s]**	**CFL [-]**	**Time step $*1e^{-8}$ [s]**	**CFL [-]**
1.1	6	6.67	1	3	0.45
	8	6.67	1	2	0.3
1.38	6	6.67	1	6	0.9
	8	6.67	1	2.5	0.37

Table 2: Time-step used at the beginning and end of each simulation with their respective CFL number.

3.2 Simulation convergence

Unlike steady computations, unsteady ones never reach proper convergences, the simulation runs as long as it is not stopped. Over time, the flow establishes itself, then turbulence takes place, the wake will keep oscillating forever. Hopefully, this oscillation motion can oscillate in a period manner. To do this, it is very useful to look at the lift coefficient of the blade. Fig. 11 shows the lift coefficient of the blade with respect to the through flow time. One through flow time T_s corresponds to the time it takes for one particle to flow over the blade.

As it can be observed, the flow has a sinusoidal behavior, at the beginning, not much happens. Then, the turbulence begins to settle at the level of the trailing-edge under the form of a Von Karman street, which produces high amplitude variation. After a relatively important period of time, big vortex shedding leaves room for much smaller turbulence, who have a less regular behavior. The amplitude of lift coefficient starts to decrease, and it eventually reaches a Limit Cycle Oscillation (LCO). At this moment, the unsteady simulation is considered to be converged and the calculations of averages can begin.

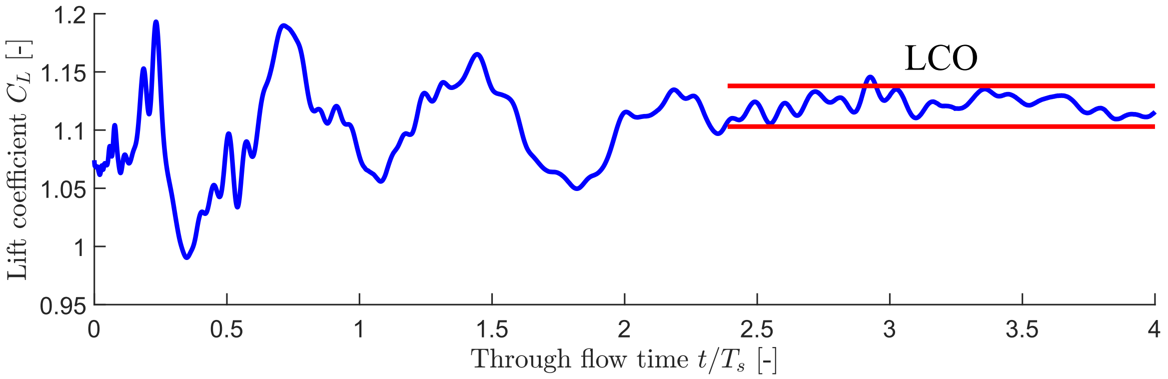

Figure 11: Evolution of the lift coefficient with respect to the through flow time.

3.3 Inlet Mach number

As said earlier in Section 2.3, imposing the total pressure from Eq. 7 at the inlet results in a Mach number that differs from the desired one. As the flow develops over the blade and the boundary layer grows, losses increase, modifying the Mach number. Fig. 12 shows the time-averaged Mach number over the inlet.

It is particularly complicated to adjust perfectly the inlet total pressure to match the target inlet Mach number. When the flow is completely developed, small modifications take a lot of computational time to be noticeable. Indeed, a change at the inlet needs a lot of computation to change the flow. And once the flow has been changed, it takes even longer to evacuate the solution from the domain. It requires tens of through flow time to stabilises. As it can be observed, the Mach number for all cases is relatively close to the target one. For the low solidity blade, shown in Fig. 12a, the differences are -1.1 % and 1.4% in average respectively for 6°and 8°incidence. For the higher solidity blade, shown in Fig. 12b, the differences are -1.3 % and 0.9% in average respectively for 6°and 8°incidence.

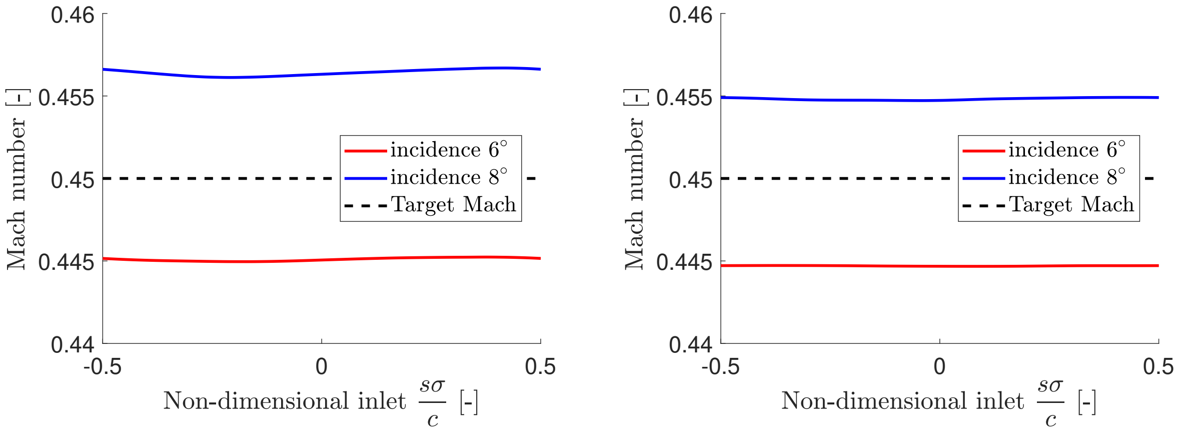

(a) Solidity σ = 1.1 (b) Solidity σ = 1.38

Figure 12: Time-averaged Mach number plotted over the inlet for both incidences and blades geometries.

In conclusion, the numerically obtained Mach numbers are very close to the objective. The velocity profiles at the inlet are very smooth, which indicates that it is located far enough from the blading not to be disturbed. Also, getting a more accurate Mach number at the input will not yield better results. Since the data shown is, in most cases, normalized to the inlet. In this case, variations of the order of one percent are acceptable. Moreover, the numerical data are confronted with experimental data, which are also subject to inaccuracies at the level of the input velocity.

3.4 Mesh resolution

The target values for the non-dimensional mesh size, required in the boundary layer, are depicted in Fig. 13. The direction normal to the surface is n and s represents the size of the circumscribed circle around the mesh element in the tangential direction. Wall spacings are non-dimensionalized using the wall shear stress τ as

$$\Delta n^+ = \frac{\rho \Delta n u_\tau}{\mu}, \text{ with } u_\tau = \sqrt{\frac{\tau}{\rho}}. \tag{9}$$

Accounting for the degree of the simulations, it would correspond to an effective non-dimensionalized resolution of $\Delta n^+_{eff} = \Delta n^+/p = 1.66$ and $\Delta s^+_{eff} = \Delta s^+/p = 6.66$.

Instantaneous contours of the n^+ field are shown in Fig. 14 and Fig. 15 respectively for solidities $\sigma = 1.1$ and $\sigma = 1.38$. The blading is seen from a position tilted three quarters to the side. The leading-edge is at the bottom and the trailing-edge above.

The stagnation point is located below the LE on the pressure side. The flow which must then pass over the LE accelerates very quickly, and strongly. It is a region where n^+ values reach a maximum. It is very difficult to reach target resolution in this particular region. In this case, the maximum value is only one order of magnitude greater than the rest. Moreover, it does not create any problems as it is localized on very few elements.

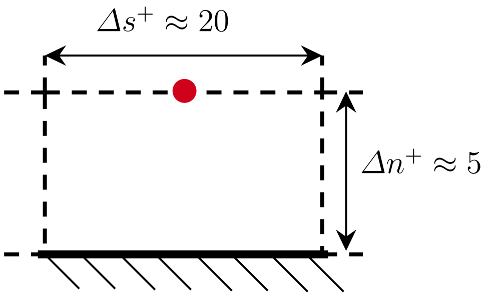

Figure 13: View representing the first mesh element near the airfoil with the target non-dimensional dimensions.

It can be observed that the flow in the pressure side remain laminar, this results in a n^+ which remains constant along the blading. On the suction side, the end of the laminar region is clearly demarcated by the sudden rise in the values.

Inside the transition region, without counting the leading edge, it is where the values are the largest on the blade. This region is dominated by low density and high wall shear stress. Which, regarding Eq. 9, is favorable for the increase of friction velocity u_r and thus n^+. Also in this region, some overshoots can be observed, where the value is locally twice as high. These overshoots are very local in space and time and are therefore absorbed in the mean. This phenomenon can be observed looking at the time-averaged n^+ and s^+ fields in Appendix A.

Instantaneous contours of the s^+ field are shown in Fig. 16. Overall, the behavior is the same as for n^+. The main differences are visible near the stagnation point, where s^+ reaches its maximum value. While n^+ tends to decrease along the airfoil, s^+ remains almost at the same value. Also, while n^+ is relatively very small on the pressure side, s^+ is more around 30. While on the suction side, higher and lower values constantly alternate due to the turbulent nature of the flow.

Values of n^+ and s^+ are respectively shown in Fig. 15a and Fig. 17a for the case at a solidity $\sigma = 1.38$ and incidence $i = 6°$. It should be noted that they are both very low. This is due to the fact that the turbulence has not yet settled correctly on the blading. The spanwise line that can be observed are Tollmien-Schlichting waves. They are at the junction between the stable laminar flow and the beginning of the turbulent flow. These are waves that originate and propagate from the trailing-edge to the leading-edge. It is a very long process, and in such a flow condition, the boundary layer is relatively thin and stable. Which means that these waves do not travel very fast.

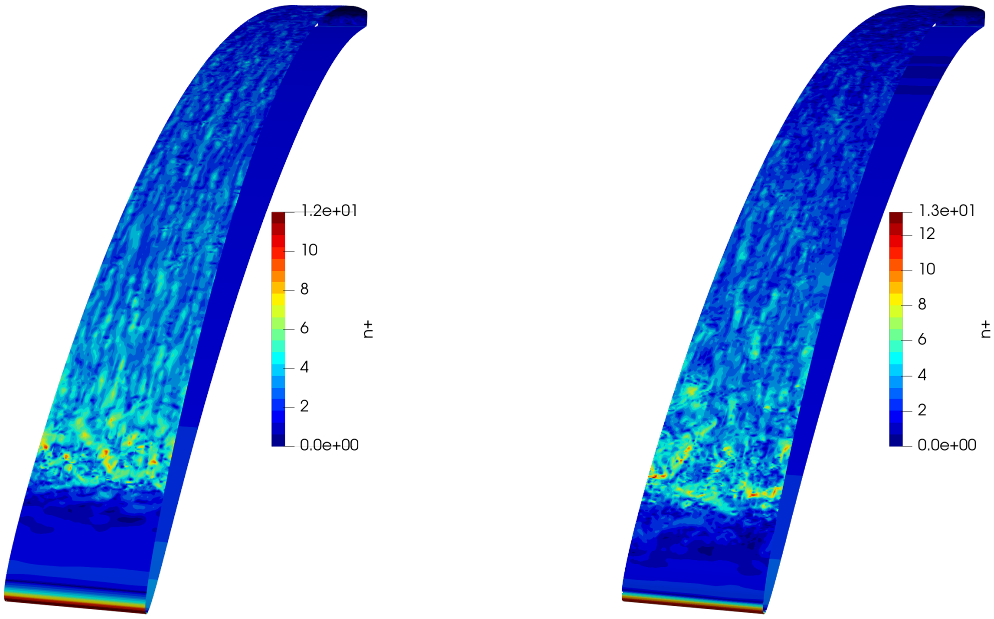

(a) Incidence i = 6°

(b) Incidence i = 8°

Figure 14: Instantaneous n^+ field over the blade surface for solidity $\sigma = 1.1$ and both incidences. Contours are shown with 20 subdivisions.

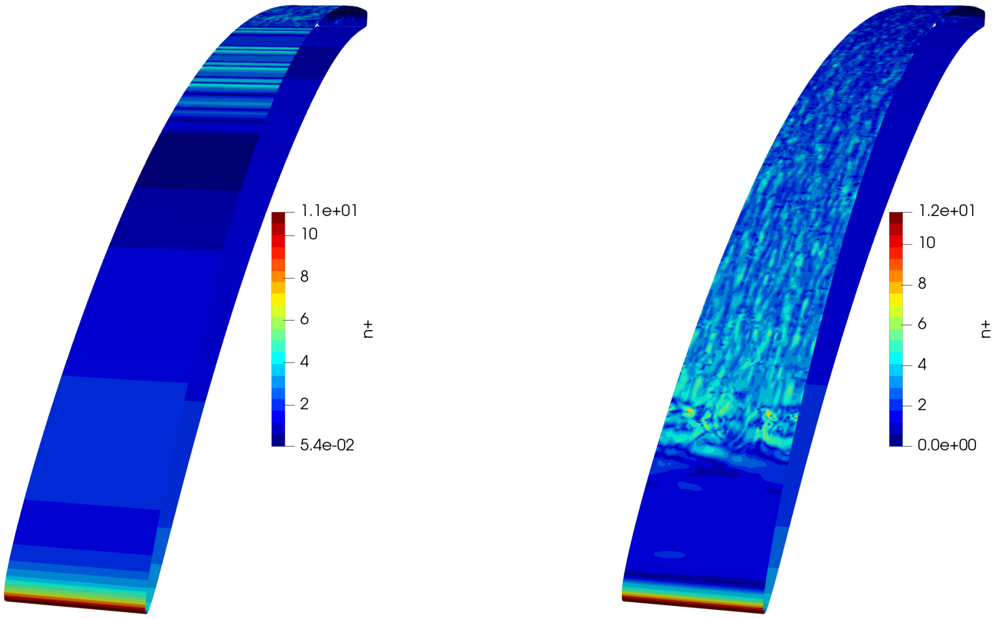

(a) Incidence i = 6°

(b) Incidence i = 8°

Figure 15: Instantaneous n^+ field over the blade surface for solidity $\sigma = 1.38$ and both incidences. Contours are shown with 20 subdivisions.

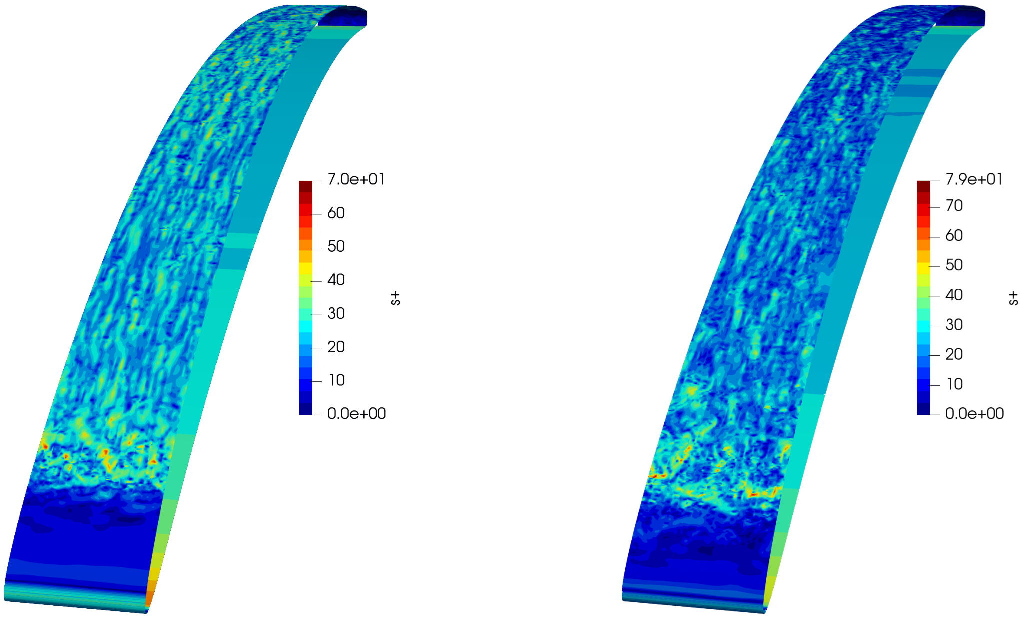

(a) Incidence i = 6°

(b) Incidence i = 8°

Figure 16: Instantaneous s^+ field over the blade surface for solidity $\sigma = 1.1$ and both incidences. Contours are shown with 20 subdivisions.

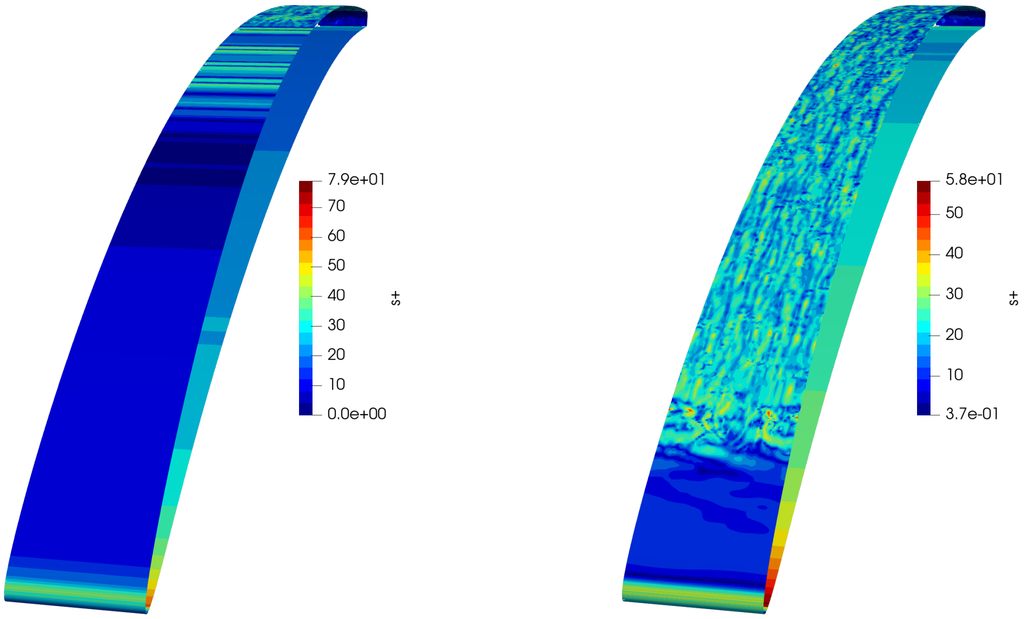

(a) Solidity σ = 1.38 and incidence i = 6°

(b) Solidity σ = 1.38 and incidence i = 8°

Figure 17: Instantaneous s^+ field over the blade surface for solidity $\sigma = 1.38$ and both incidences. Contours are shown with 20 subdivisions.

Tab. 3 shows the weighted average of the n^+ and s^+ fields. They are rather close to the target values that were shown in Fig. 13. In the case of n^+, the transition region is relatively large and tends to push the average up. On average, the value of $n+$ is more than twice lower than the target value. Considering that is order three, the mesh size normal to the surface is thin enough to capture all the scale of the turbulence. In the transition zone, there are effective values of the order of $n^+ = 1.5 - 2$ which is perfectly acceptable. On the rest of the blading, the boundary layer is even slightly over-resolved.

For the s^+, the computed average values are also good in average. The average is a little misleading in the sense that it is pulled up due to the pressure side. The suction side has s^+ in average that are smaller. A tangential resolution of the order of 20 is not sufficient to perfectly capture the smallest turbulent structures. But it remains a very acceptable value, which is not far from the target value.

Overall, the mesh quality on the airfoil, is good in the normal direction and reasonably good in the tangential direction.

Solidity σ [-]	**Incidence [°]**	n^+_{avg} **[-]**	s^+_{avg} **[-]**
1.1	6	1.75	22.99
	8	1.66	21.81
1.38	6	1.69	20.22
	8	1.76	20.13

Table 3: Weighted average of n^+ and s^+ over the blade.

For the extrusion resolution, s^+ fields from Fig. 16 already gives a good estimate of the spanwise resolution, but is not enough. This information is complemented by looking at the continuity of the different field on the surface. If the mesh resolution is not fine enough, the DGM method will cause a sudden jump in value at the mesh boundaries. The coefficient of friction is a good indicator of the continuity of the surface flow field. Therefore, if the skin friction is not continuous, then n^+ will not be either.

A close up view of the airfoil with the n^+ field, is shown in Fig. 18, with zooms on the LE, TE and a bit before mid-blade. The flow considered is the one who is most prone to being discontinuous, which is for solidity $\sigma = 1.1$ and incidence of 8°. It can be observed that the flow field is very smooth and continuous everywhere. Some very small discontinuities can be seen in the transition region near the LE. In two dimensions, the continuity of the flow field inside the domain corroborates the mesh resolution around the blade and in the wake.

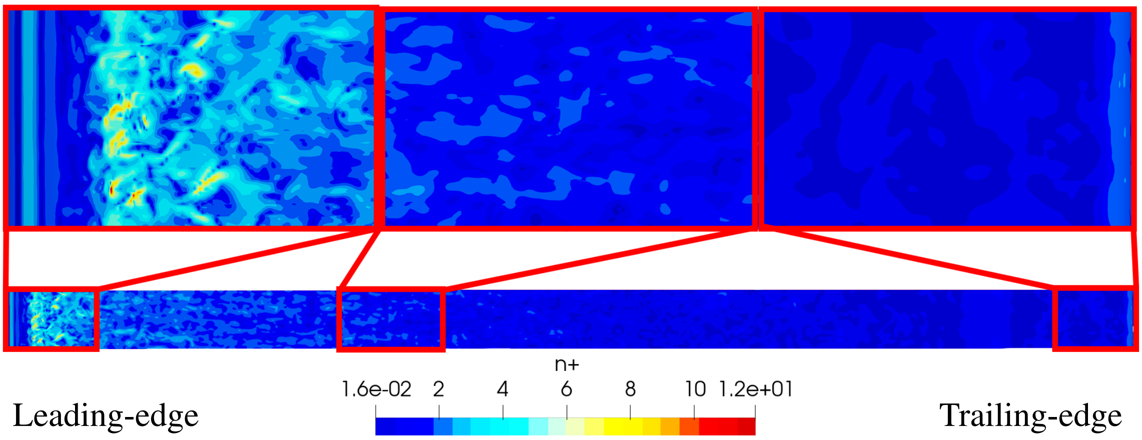

Figure 18: Instantaneous n^+ field over the suction side of the blade, with three zooms in different region, to see if the blade is free of major discontinuities.

3.5 Spatial velocity correlations

As it was said before, the extrusion distance of the domain in the direction z is 5% of the chord. This distance cannot be taken arbitrarily. In fact, it must be large enough so that the periodic planes do not have an impact on the flow. Ideally, the velocities at mid-span should be perfectly uncorrelated, i.e. the spatial velocity correlation at mid-span should be equal to zero.

The spatial velocity correlations are equivalent to a two-point autocorrelation, which is defined as

$$R_{mm}(\mathbf{x}, \mathbf{r}, t) = \langle u'_m(\mathbf{x}, t) u'_m(\mathbf{x} + \mathbf{r}, t) \rangle \tag{10}$$

where $\mathbf{r}$ is the correlation distance and x the position of the considered particle. The index m corresponding to the component u, v or w of velocity vector. The velocity correlations are then time-averaged.

The spatial correlation is calculated on a probe grid. This probe grid is constructed by double extrusion from the blade profile. The flow case chosen to illustrate this process is the first case carried out for this study. Which corresponds to a solidity of $\sigma = 1.1$ and an incidence of $i = 6°$. The probe set is extruded by 5% of the chord in a direction normal to the profile of the blade, which more or less corresponds to the thickness of the boundary layer at the trailing edge.

Such a probe grid is shown in Fig. 19, it corresponds to a point cloud. The coloring of the point represents the spanwise velocity correlation. For a point on the probe grid, three spatial correlations are calculated using Eq. 10, one in each direction. Each point is therefore evaluated, taking into account the distance from all other points.

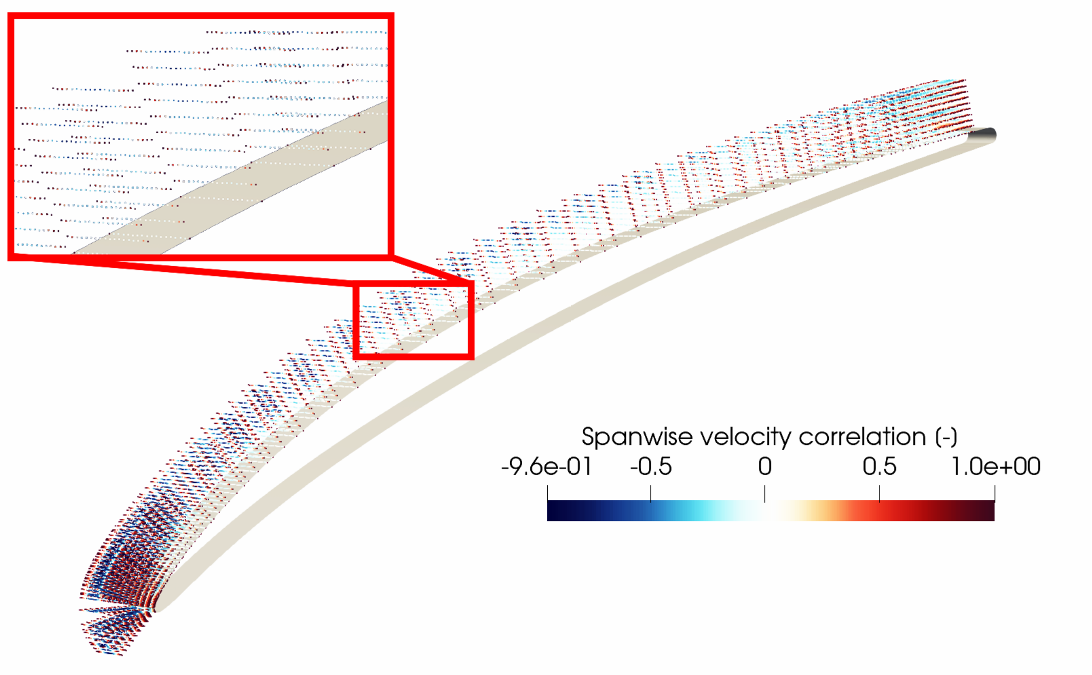

Figure 19: Probe grid, resulting from a double extrusion of the set of points that defines the blade. The coloring represents the spanwise velocity correlation.

The velocity correlations are extracted at the mid-span from the LE to the TE and shown in Fig. 20. Three different heights from the wall are considered and are indicated by a fraction of the maximum boundary layer height δ measured at the TE. It can be seen that, for every direction, the velocities are very well decorrelated, since at 0% and 20% of δ, the correlation is almost zero everywhere.

In any case, it can be seen that the correlation is almost perfect at the beginning. This is due to the laminar bubble, which is located at the LE.

The green curve corresponds to a height of 40% of δ. Fig. 20a shows the chordwise correlation. Near the TE, fluid particles are correlated quite a lot. This is due by the fact that turbulent structures are quite elongated in this direction, and thus it is more difficult to obtain no correlation. This phenomenon is not observed when looking at the vertical correlation in Fig. 20b because turbulent structures are thinner. When looking at the spanwise correlation in Fig. 20c, particles seems to be highly correlated. At the start of blading, the height considered is outside the boundary layer. Therefore, the correlation is perfect. Further along the blading, the correlation decreases, but never reaches zero. This can be explained by the fact that the spanwise velocities are very small and that the flow, although turbulent, still looks like a two-dimensional flow.

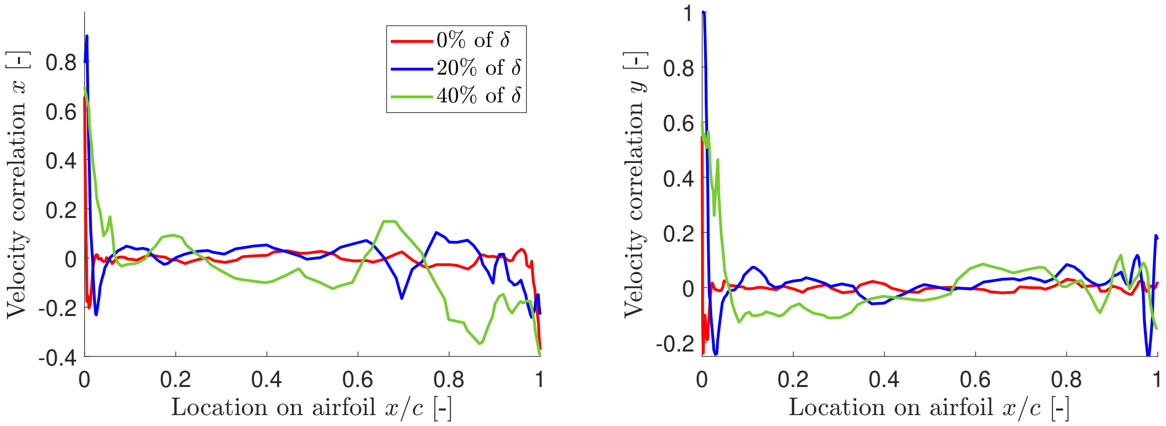

(a) Chord wise correlation x-axis

(b) Vertical correlation y-axis

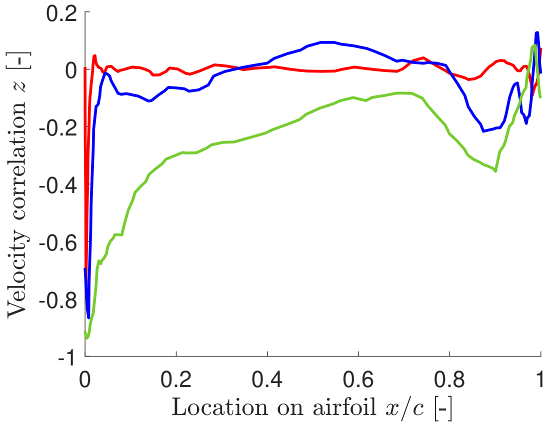

(c) Spanwise correlation z-axis

Figure 20: Velocity correlations extracted at the mid-span shown in non-dimensional coordinates from TE to LE for three different height in the boundary layer.

The analysis made just before shows whether the velocities are uncorrelated at mid-span. But it gives no information about the extent along the span. To do this, the span-wise velocity correlation is shown along the span in Fig. 21. Three different location are considered as well as three different height in the boundary layer.

The red curve shows the correlation on the surface, at the LE and mid-span, the velocities are uncorrelated all along the span. At the TE, shown in Fig. 21c, the particles are not correlated over a portion of 60% of the span.

Considering the blue and green curves, they show on Fig. 21a and Fig. 21a a no correlation region of half the span. This effect is greatly diminished when looking high into the boundary layer at the TE shown in Fig. 21a.

To sum up, the analysis made shows that a span of 5% of the chord is sufficient to guarantee that the periodic walls have no influence on the flow. Although the decorrelation is not perfect at the TE, it remains small and localized enough to not compromise the results.

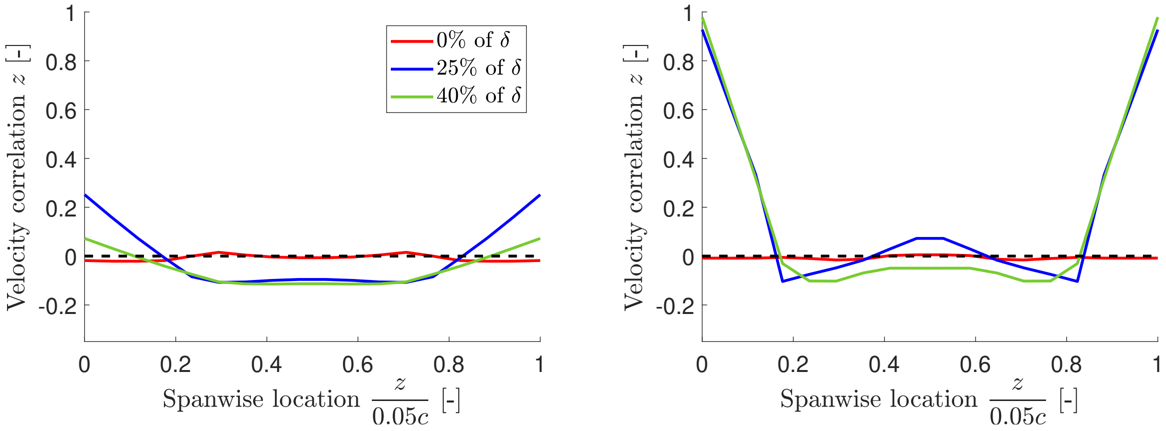

(a) Located at 7% of c

(b) Located at mid-span

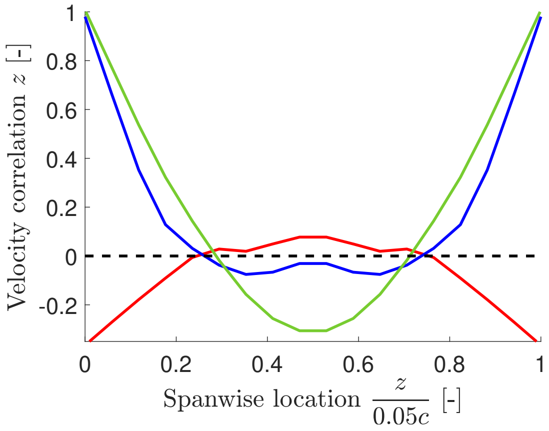

(c) Located at TE

Figure 21: Spanwise velocity correlation along the span extracted at three different positions on the blade for three different height in the boundary layer.

4 Results

This section details instantaneous and time-averaged results computed for every computational cases. The time-averaging is obtained by sample mean of the considered field, where a sample is created for each calculated time step. It is computed as

$$\bar{X} = \frac{1}{N}\sum_{i=1}^{N} X_i, \tag{11}$$

where N is the total number of sample and X is the considered field.

First, the numerical results are compared with each other. Then, the numerical results are compared with the experimental results provided by Safran Aero Boosters. These are two experiments aimed at calculating the loss coefficient of the blade cascade and outlet flow angle. The results are available in the Appendix B, two solidities and three incidences were carried out.

Fig. 22 shows the spanwise velocity v_z contours of the flow field. It shows a general overview of the behavior of the flow around the blading. The flow is characterized by a thick boundary layer. As it was already observed in Section 3.4, the flow on the pressure side remains laminar. A general view of the cascade, with three blades, is illustrated in Appendix B.

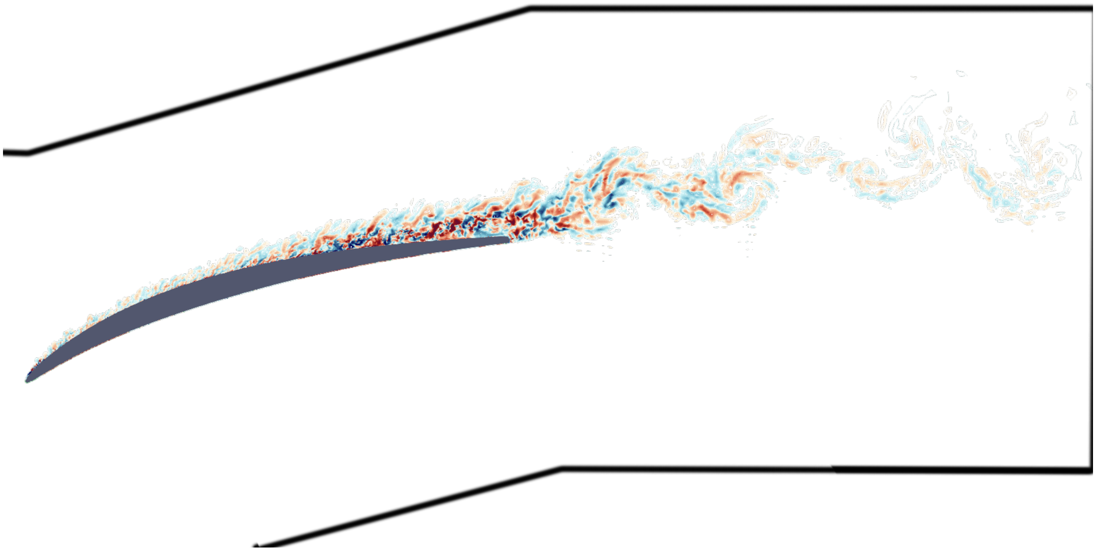

Figure 22: Instantaneous spanwise velocity v_z contours, for the case $\sigma = 1.1$ and $i = 8°$, computed on the periodic boundary. Positive values are in red and negative are in blue. inflow turbulence

4.1 Flow features

This section details the different flow features for every flow conditions. It also provides an in-depth analysis of the flow around the leading edge and through the cascade.

In general, the flow conditions corresponding to $i = 6°$ and $\sigma = 1.1$, $i = 8°$ and $\sigma = 1.1$ and $i = 8°$ and $\sigma = 1.38$ are respectively named case 1, case 2 and case 3 for convenience. Flow around the blade is analysed using time-averaged velocity field available in Appendix D and skin friction in Appendix C.

4.1.1 Overview of flow fields

The flow field near the leading-edge and around the blades is very different for each case. To better highlight these differences, Fig. 23 shows an overlay of the contours of the boundary layer for the three cases.

On the left, the figure represents a zoom, corresponding to 7% of the chord, on the leading edge. The dotted lines show the moment when the laminar bubble ends. In general, the size of the laminar bubble is relatively similar for case 1 and 3. Case 2 shows the tallest and shortest bubble.

On the right, the Fig. 23 represents the whole blade. The solid lines represent boundary layer contours. Case 2 shows the thickest boundary layer, and reaches a height of 10% of the chord at the trailing-edge. The two other cases are half as thick.

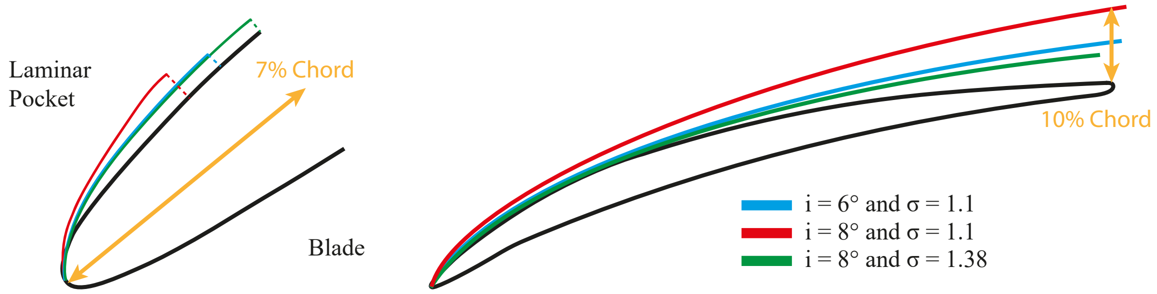

Figure 23: Representation of the contour of the laminar pocket and its extent (on the left) and contours of the boundary layer (right) for the three flow conditions.

4.1.2 Laminar separation bubble

A three-quarter view of the leading-edge with the time-averaged skin friction on the solid surface and the time-averaged velocity streamlines on the periodic plane is shown in Fig. 24. It illustrates a lot of processes, the flow arrives at the bottom and hits the blade at the stagnation point. From it, a laminar boundary layer develops and slowly thickens. After the LE, there is a separation point, where the streamlines are dividing. Because of this separation, there is a fairly elongated zone where the air is stagnant, which is a laminar separation bubble. At the end of the separation bubble, a recirculation region can also be observed.

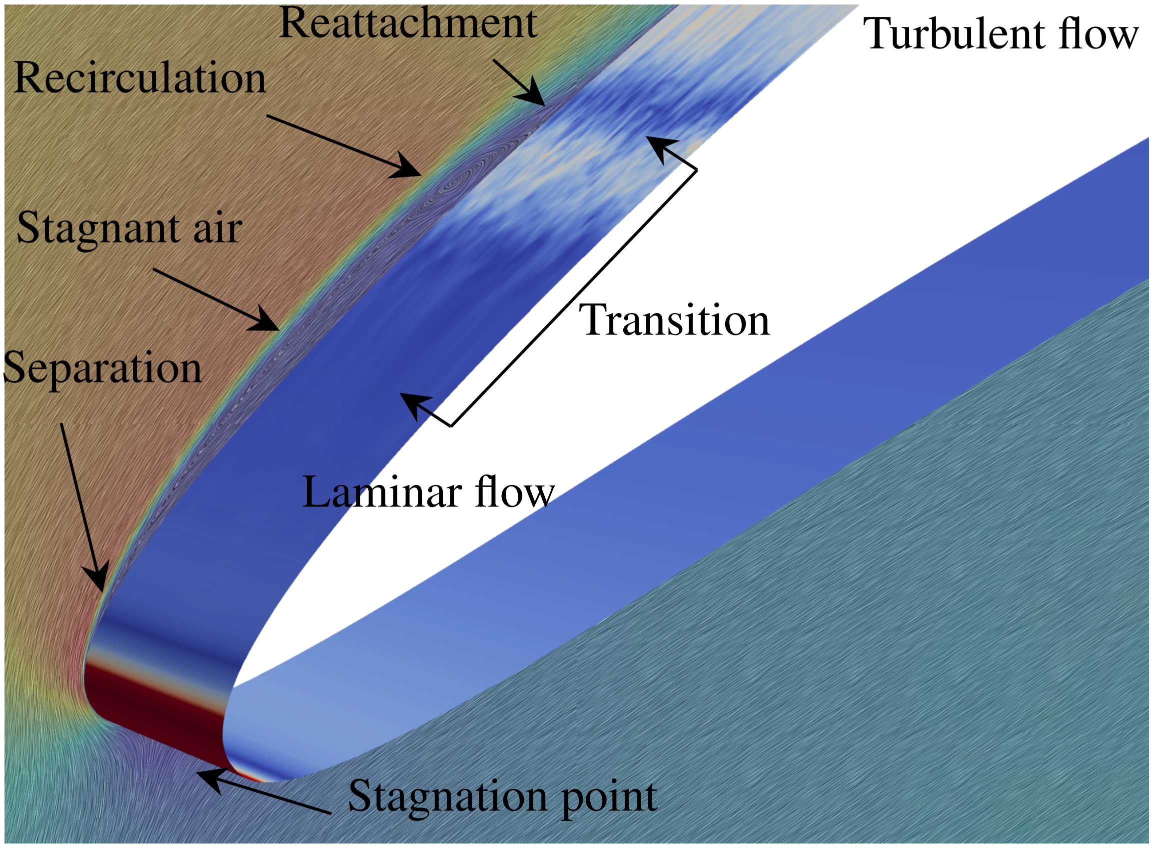

Figure 24: Three-quarter view of leading edge with the time-averaged skin friction on the solid surface and the time-averaged velocity streamlines on the periodic plane. Zero values are indicated in blue while high values are indicated in red.

After the recirculation zone, the flow reattaches to the wall. Attachment to the wall can be observed by a sudden drop in the coefficient of friction (which turns blue). One thing to be noted here is that the flow reattaches when the transition has already begun. Then, the flow becomes fully turbulent, which is delimited by the end of the dark-blue region on the periodic surface and the sudden rise in the friction on the solid surface. The transition from laminar to turbulent is analyzed in more detail later in the next section.

To better put into perspective the differences between the laminar separation bubbles, Fig. 25 shows a spanwise view of the periodic plane with a zoom on the LE. The zoom represents an 8.4% portion of the agreement. The values correspond to the streamlines of the time-averaged velocity field. The figure shows the length and width of the bubble, the dimensions are expressed in percentages of the chord.

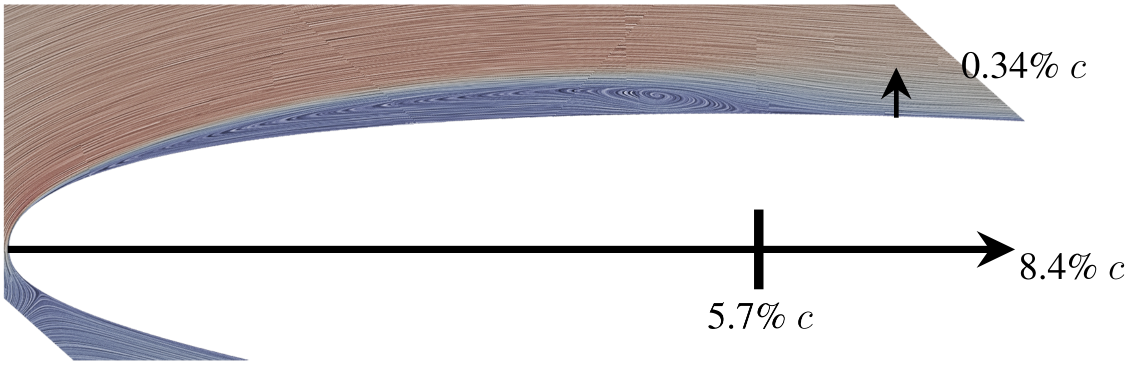

Solidity $\sigma = 1.1$ and incidence $i = 6^\circ$

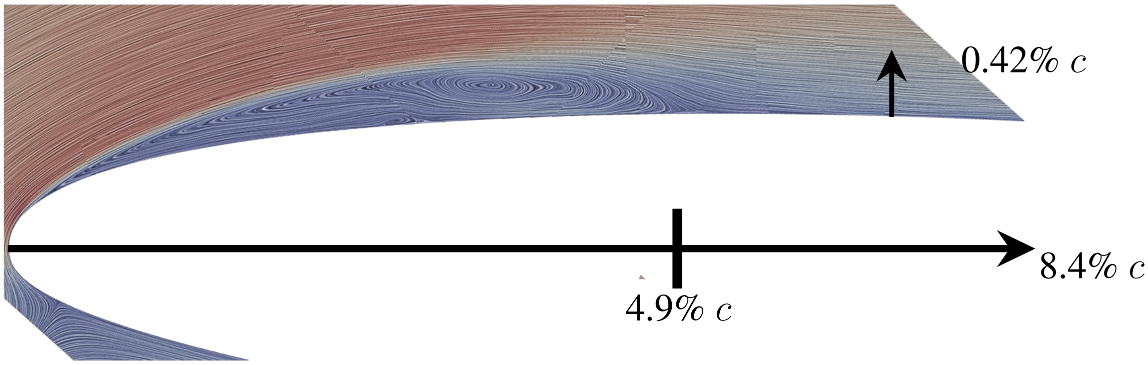

Solidity $\sigma = 1.1$ and incidence $i = 8^\circ$

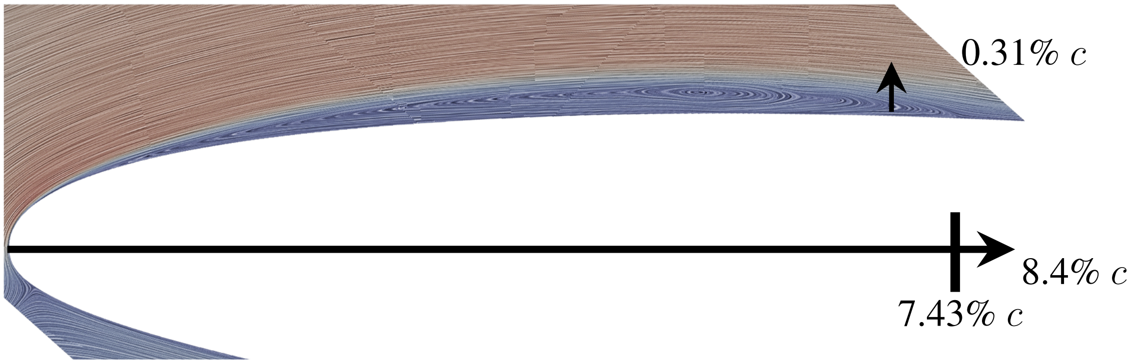

Solidity $\sigma = 1.38$ and incidence $i = 8^\circ$

Figure 25: Spanwise view of the periodic plane, with a zoom on the laminar separation bubble, for different flow condition.

The first thing that can be observed, is it that for the first and third case, the heights of the LSB are nearly the same in height. The second case has the thickest bubble, which is 23% bigger than the first case and 35% bigger than the third case. They are also both very elongated along the chord. The second case has a bubble that is 15% shorter than the first case and 35% shorter than the third case. One thing to be noted is that both the first and third cases have only one recirculation vortex, while the second case has a smaller recirculation vortex that is approximately at the middle of the bubble.

4.1.3 Laminar to turbulent transition and flow separation

The study of the transition from laminar to turbulent makes it possible to better understand the differences between every incidences and solidities. As a quantitative estimate, the skin friction for each of the cases is shown in Fig. 26. On the left is the spanwise instantaneous ($z-axis$) component of the friction, and on the right is the time-averaged skin friction magnitude. Light brown represents zero, blue represents negative values and red represents positive values. A complete view of time-averaged skin friction in logarithmic scale is available in Appendix C

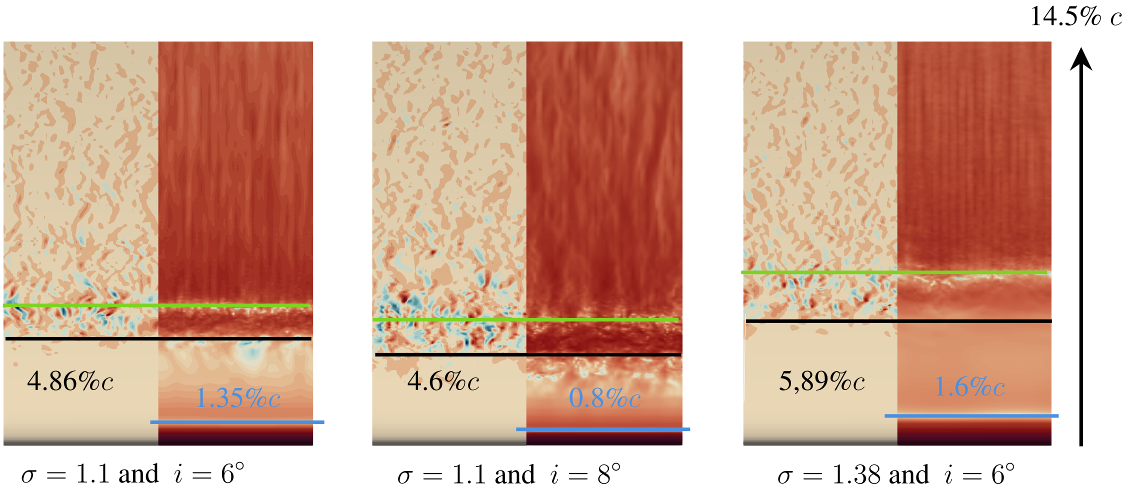

Figure 26: Front view of the leading flow, the zoom represents nearly 15% of c. On the left, the instantaneous z component of the skin friction and on the right, the time-averaged skin friction magnitude for each flow conditions.

The region where the transition from laminar to turbulent begins is shown using a black horizontal bar. The green horizontal bar shows the area where the flow reattaches. For every flow conditions, the reattachment is considered turbulent as it happens at the end of the transition. Above the green bar, the flow is fully turbulent.

For the flows at a solidity $\sigma = 1.1$, the transition begins almost in the same place. For the high solidity case, the transition starts 1% of c after. This is in line with what had been observed during the analysis of the laminar bubble before. The extent of the transition region is nearly the same for every case. The only noticeable difference is the shape of the region of interest, but this is dependent on the number of samples present in the averaging. The more samples are considered, the more the demarcation of the different zones is marked.

Laminar separation is indicated in Fig. 26 with a blue line. The separation takes place in the part where the curvature of the blading is very important. In this region, a slight vertical variation is actually quite a large deviation along the blading. The separation is then done very early for the case 2 $\approx 0.8\%$ of c. For the other two, it happens later, respectively $\approx 1.35\%$ and

$\approx 1.6\%$ of c.

Laminar separation is not the only separation that can occur on the blading. One of the most important problems that affects performance of compressors is the turbulent flow separation. This separation of the boundary layer is the reason why the wake can be so big. Separation causes a drop in kinetic energy, and causes the flow to recirculate on the blading [2]. The high solidity flow does not face separation. Indeed, the fact that the flow is more constrained is a factor limiting the separation. When we look at the flow at low solidity ($\sigma = 1.1$) at low incidence ($i = 6°$), the boundary layer remains attached until the end. This is not the case at an incidence of $8°$. Streamlines of the time-averaged velocity field are shown in Fig. 27. Where the boundary layer detaching to form a large wake is clearly visible. Separation occurs at 60% of the chord. A double zoom is made on the LE where the main laminar separation bubble be seen. Another rectangle shows the position of the secondary recirculation bubble, which is difficult to see due to its very small size.

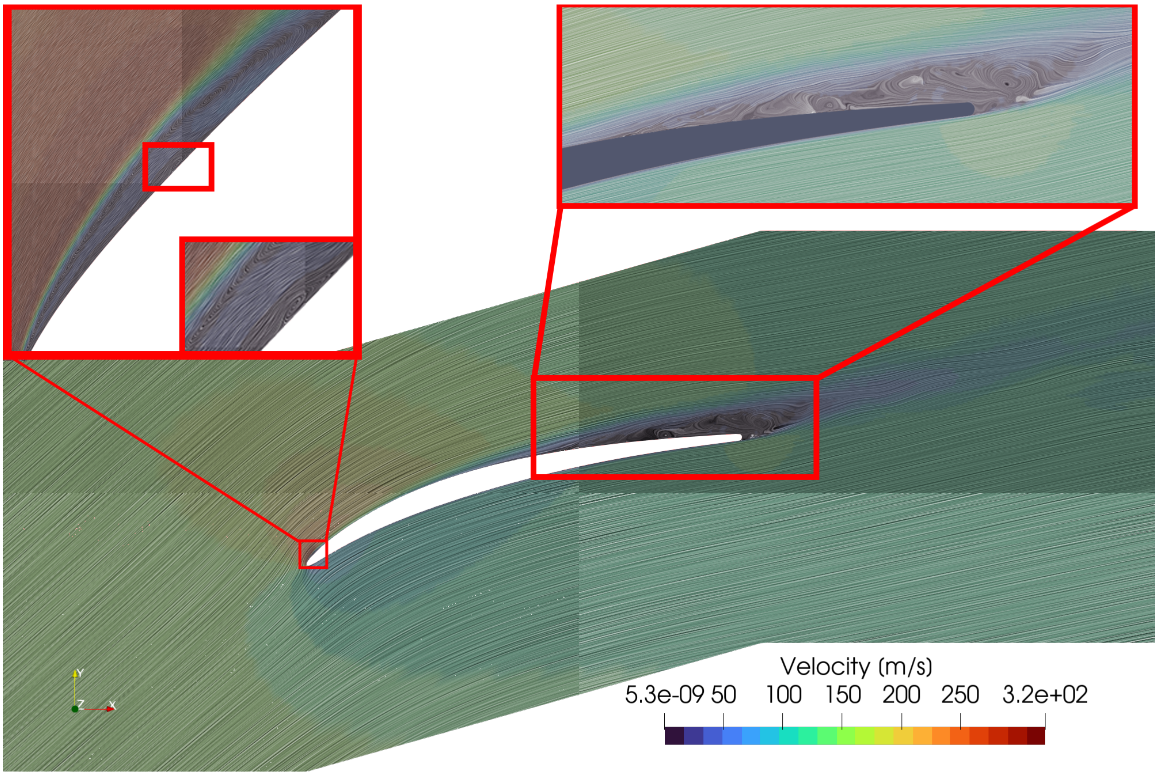

Figure 27: View of the periodic plane with the streamlines of the velocity field for the case at $i = 8°$ and solidity $\sigma = 1.1$.

The velocity profiles, corresponding to solidity $\sigma = 1.1$ and incidence $i = 8°$, are extracted normal to the surface and shown in Fig. 28 and Fig. 29. The horizontal axis represents the velocity normalized by the free stream velocity. And the vertical axis represents the height normalized by the boundary layer thickness. The velocity profiles are extracted from $x/c = 0.45$ to $x/c = 0.82$. In Fig. 28, a zoom is made on the very bottom of the velocity profile to show that $x/c = 0.65$ the is going in reverse direction near the surface. In Fig. 28, it can be observed that the flow is nearly still near the surface at, $x/c = 0.78$ then flows in reverse just after.

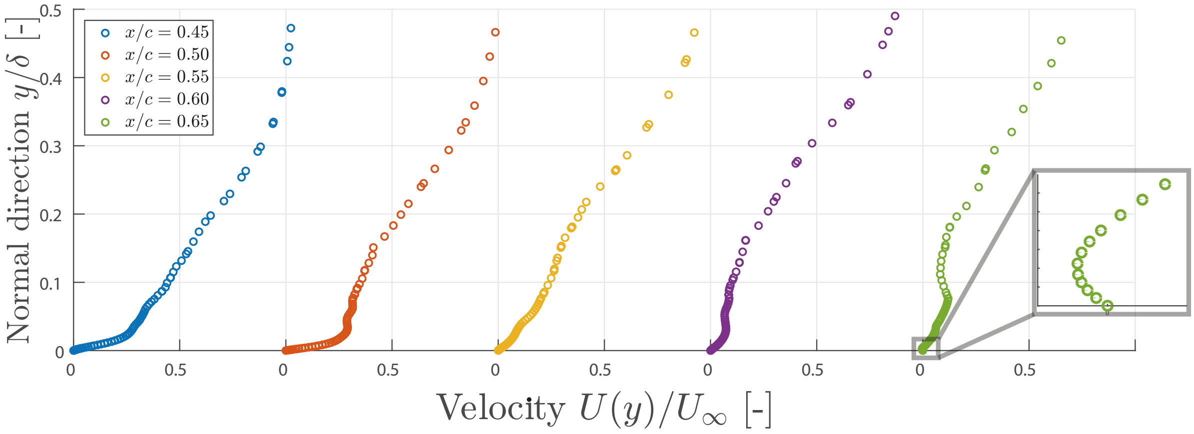

Figure 28: Velocity profile normalized to the free stream velocity along the normal direction normalized by the boundary layer thickness.

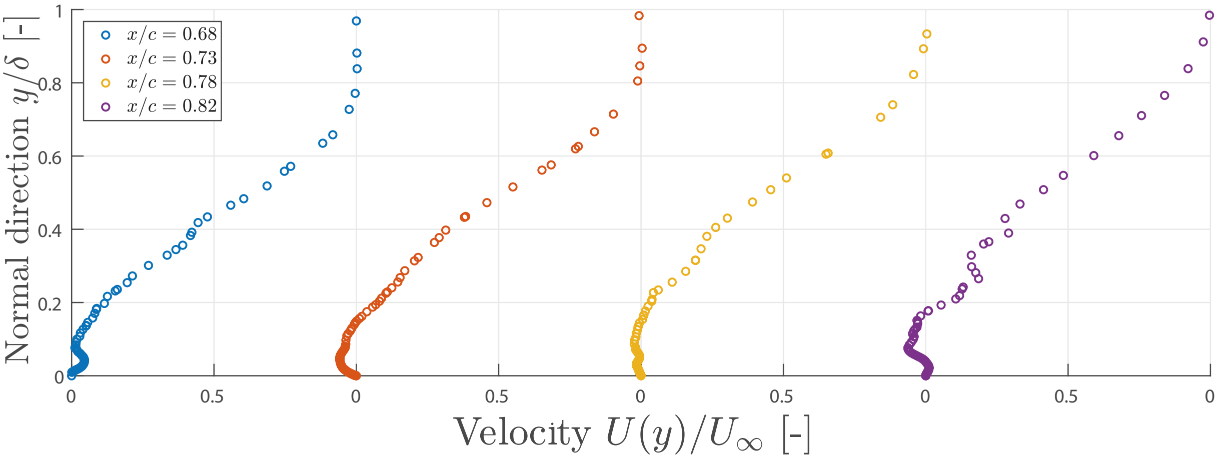

Figure 29: Velocity profile normalized to the free stream velocity along the normal direction normalized by the boundary layer thickness.

4.2 Mach number

The instantaneous Mach number (left) and time-averaged one (right) are shown in Fig. 30, Fig. 31 and Fig. 32 and correspond respectively to the flow conditions $i = 6°$ and $\sigma = 1.1$, $i = 8°$ and $\sigma = 1.1$ and $i = 8°$ and $\sigma = 1.38$.

In Fig. 30 and Fig. 32 the Mach number reaches a maximum value of approximately $M = 0.9$ at the leading-edge. The case at low solidity and high incidence, shown in Fig. 31a has a time-averaged Mach number that reaches 1 at the LE. There is a very small supersonic pocket which is just above the boundary layer.

In Fig. 31b, it can also be seen that in the instantaneous field, the Mach number can reach values slightly higher than 1. At the top of the laminar bubble, the speed is very close to Mach 1, so that when vortices escape, they accelerate suddenly and strongly. They can reach relatively high speeds, but they are very localized in space and time. They disappear very quickly and have no influence on the average. It seems that these vortices are purely numerical transient effects, due to boundary layer oscillations at the end of the laminar bubble.

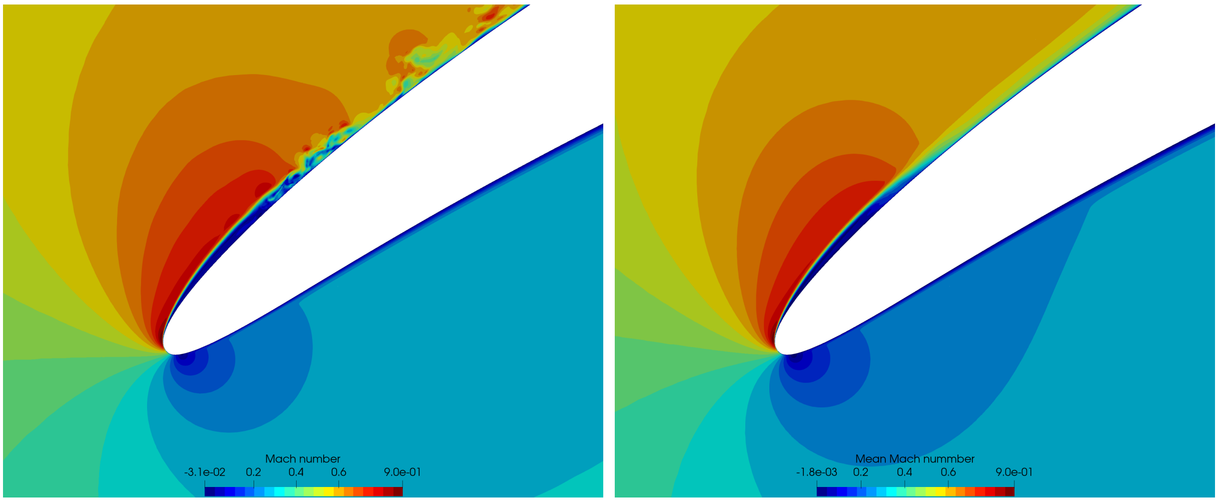

(a) Mach number M

(b) Time-averaged Mach number $\bar{M}$

Figure 30: Instantaneous and time-averaged Mach contours for $i = 6°$ at solidity $\sigma = 1.1$. Contours are shown with 20 subdivisions $M = 0$ to 0.9.

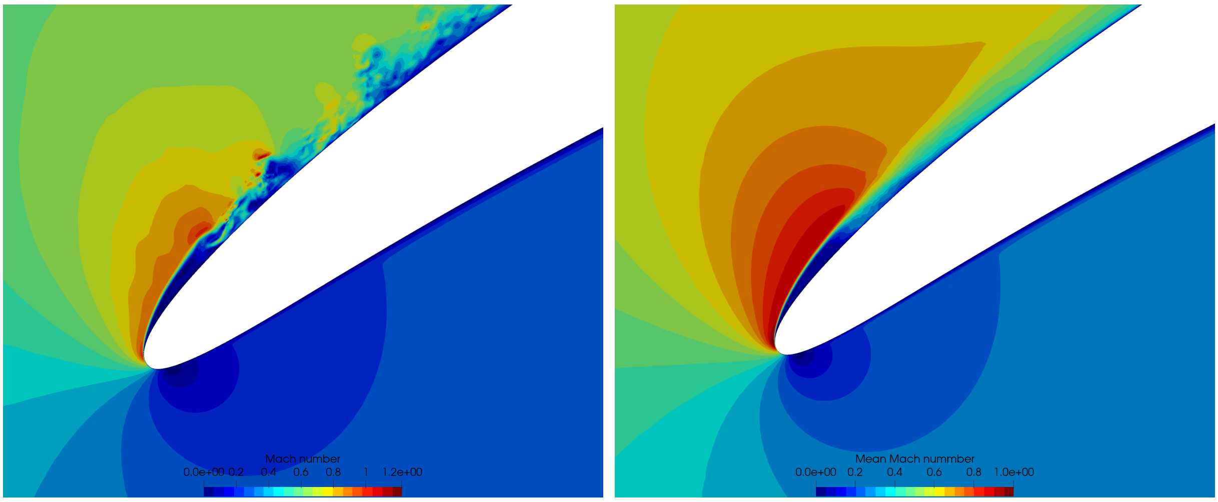

(a) Mach number M

(b) Time-averaged Mach number $\bar{M}$

Figure 31: Instantaneous and time-averaged Mach contours for $i = 8°$ at solidity $\sigma = 1.1$. Contours are shown with 20 subdivisions $M = 0$ to 1.

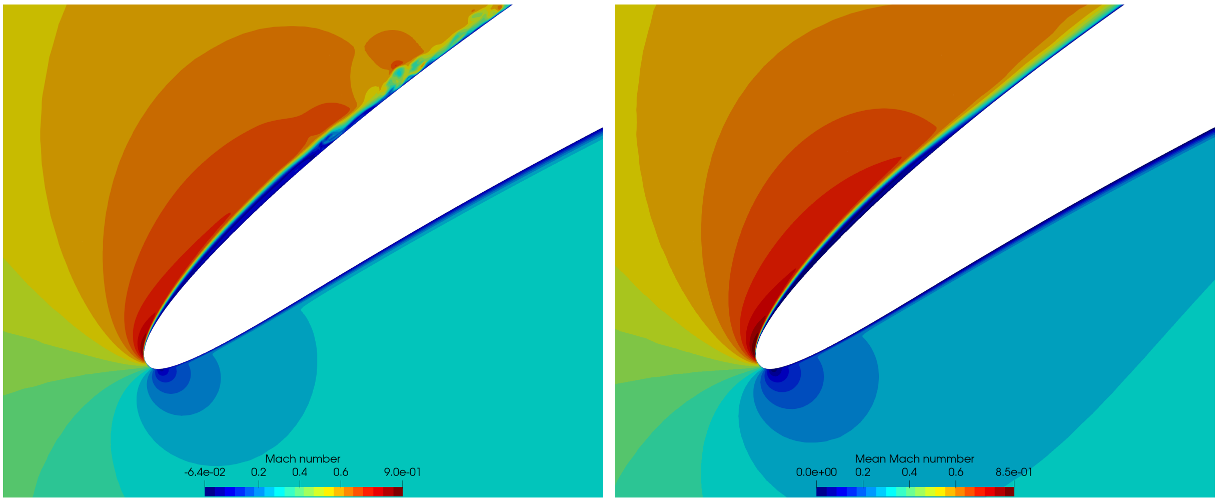

(a) Mach number M

(b) Time-averaged Mach number $\bar{M}$

Figure 32: Instantaneous and time-averaged Mach contours for $i = 8°$ at solidity $\sigma = 1.38$. Contours are shown with 20 subdivisions $M = 0$ to 0.85.

4.3 Isentropic Mach number

The isentropic Mach number is the Mach number that there would be without any losses in the flow. This property is often used to investigate the ideal surface Mach number, considering a slip condition on the blade i.e. without any wall friction. The isentropic Mach number M_{is} can be computed from the isentropic flow in pressure

$$\frac{p_0}{p} = \left(1 + \frac{\gamma - 1}{2} M^2\right)^{\frac{\gamma}{\gamma - 1}}, \tag{12}$$

where p_0 is the Total pressure in the free stream outside of the boundary layers. In this case, the inlet total pressure is used. p is the local Static pressure and γ is the ratio of specific heats, for air $\gamma = 1.4$.

The isentropic Mach number can thus be computed by rearranging Eq. 12, gives the following formulation

$$M_{is} = \sqrt{\left(\left(\frac{p_0}{p}\right)^{\frac{\gamma-1}{\gamma}} - 1\right) \frac{2}{\gamma - 1}}. \tag{13}$$

The time-averaged isentropic Mach number, over the blade in non-dimensional units, are shown in Fig. 33 and Fig. 34. The complete fields are available in Appendix H also with zooms on the LE. The isotropic Mach numbers for each of the cases are relatively close to the real ones seen in section 4.2.

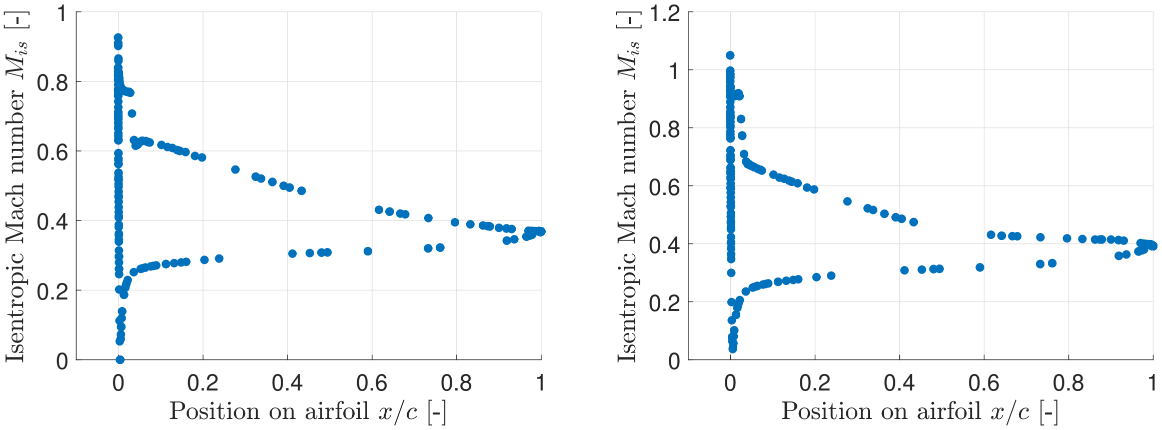

(a) $i = 6°$ and $M_{is,max} = 0.93$ (b) $i = 8°$ and $M_{is,max} = 1.05$

Figure 33: Isentropic Mach number extracted on the blade, resulting from time-averaged static pressure. The blade solidity is $\sigma = 1.1$ for both flow incidence.

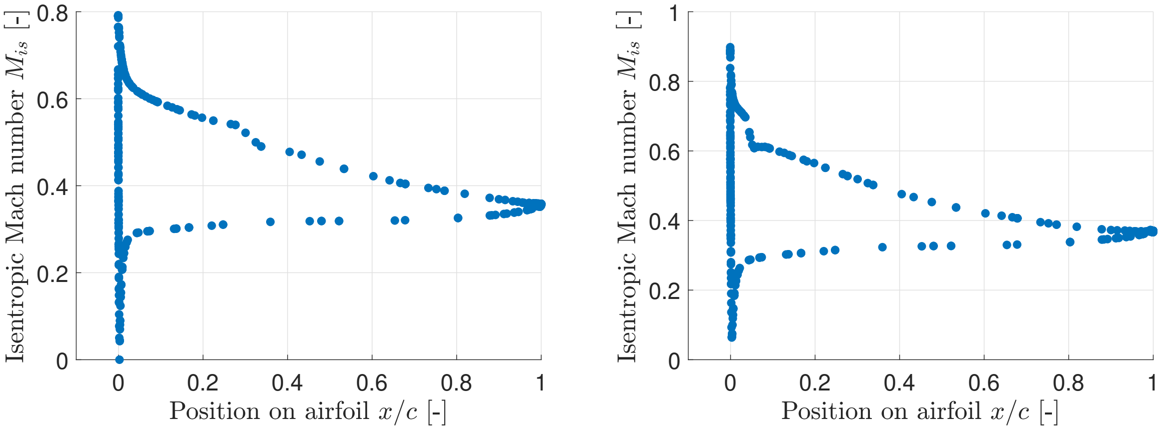

(a) $i = 6°$ and $M_{is,max} = 0.8$ (b) $i = 8°$ and $M_{is,max} = 0.9$

Figure 34: Isentropic Mach number extracted on the blade, resulting from time-averaged static pressure. The blade solidity is $\sigma = 1.38$ for both flow incidence.

4.4 Losses in the cascade

The flow inside a turbo machine is three-dimensionnals, viscous and compressible. Such a complex flow is associated with total pressure loss once the flow has passed the blade. The loss coefficient can be straight-fully computed by comparing the total pressure before and after the blade. As a general rule, the reference kinetic energy is taken to be the highest value outside the cascade, i.e. upstream for compressors [8].

The losses are thus computed as

$$C_\eta = \frac{p_{0,i} - \overline{p}}{p_{0,i} - p_{out}}, \tag{14}$$

where $p_{0,i}$ is the inlet time-averaged total pressure, $\bar{p}$ is the integrated time-averaged total pressure, which is integrated normalized by the mass flow as

$$\bar{p} = \frac{\int \rho v_x p(y) dy}{\int_i \rho v_x dy} \tag{15}$$

over the plane where the measurement station is located. And p_{out} is the outlet static pressure.

An integration as shown in Eq. 15 is more suitable than a regular surface integration. Indeed, for the low solidity case, at $\sigma = 1.1$, losses integrated over the surface produce results that are more than 3 times higher than when weighting the integration by the debit.

A view of the cascade is displayed in Fig. 35. The loss coefficient is computed at two different stations, the first one is at the trailing-edge. The second one is half a chord after the trailing-edge, which correspond to ≈ 48.3 [mm] downstream of the leading-edge. It is carried out in this way in order to correspond to a simulation campaign carried out previously on the same blading by [4]. The latter compares experimental data carried out in the tunnel with Large Eddy Simulations.

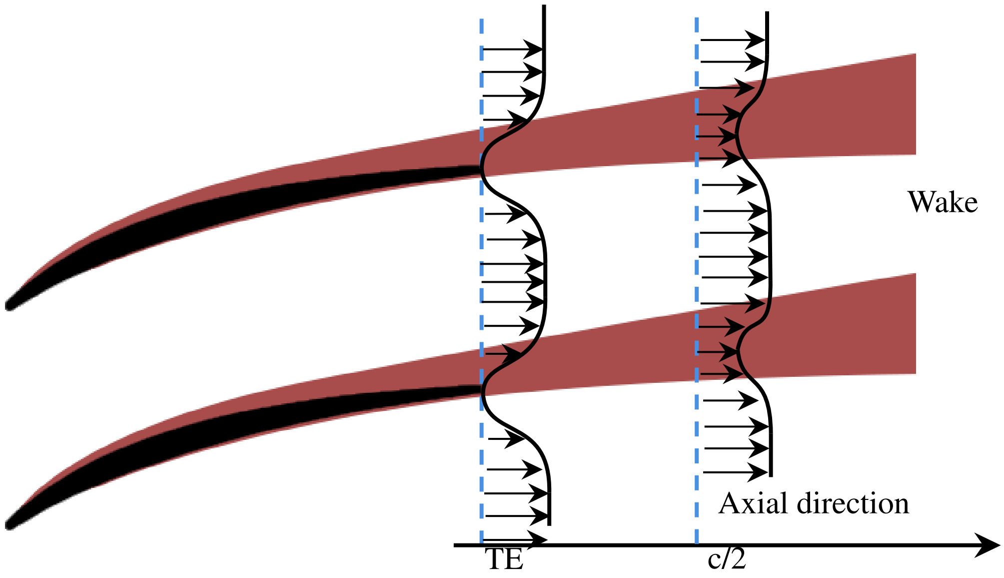

Figure 35: Wake development with the two stations of reference where losses are computing in the cascade.

The time-averaged total pressure can be found in Appendix E. Tab. 4 summarizes the integrated total-pressure losses at both stations. For the low solidity cascade, the losses are multiplied by a factor three between the incidence at 6°and 8°.

Comparison of loss coefficients of experimental data and DNS data is shown in Fig. 36. In order to accommodate the quadratic profile of the losses, a second order curve fit is done on experimental data, at a solidity $\sigma = 1.1$, using a least-squares method. As it can be observed in Fig. 36a, DNS data are relatively close to experimental ones. Numerical data shows a difference

		Loss coefficient	
Solidity σ [-]	**Incidence i [°]**	**TE** [-]	$c/2$ **[-]**
1.1	6	0.0343	0.0234
	8	0.1249	0.0691
1.38	6	0.0195	0.0108
	8	0.0535	0.0297

Table 4: Integrated wake losses over the two stations located at the trailing-edge and half a chord behind.

of -10% and -13% respectively for incidences of 6°and 8°.

For the cases at solidity $\sigma = 1.38$, only two experimental incidences are available. A comparison of a first order curve fit from experimental data and DNS results is shown in Fig. 36b. Numerical results obtained at 6°incidence are way underestimating the losses through the cascade. Indeed, the boundary layer is not developed completely yet, and the wake is this thinner than it should be. For the 8°case, numerical losses are a bit overestimating experimental ones. Overall, numerical computation shows a difference of -37% and -13% respectively for incidences of 6°and 8°.

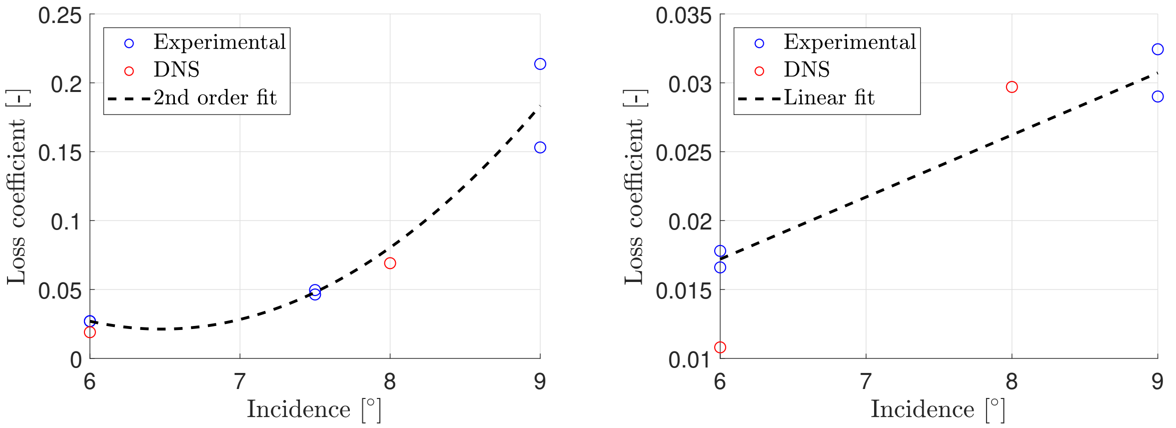

(a) Solidity $\sigma = 1.1$ (b) Solidity $\sigma = 1.38$

Figure 36: Comparison of loss coefficients of experimental data and DNS data.

4.5 Flow angles

Compressor cascade tends to turn the flow in the direction of rotation, in this case, in the camber direction. The flow angles can be used to determine whether the cascade perform as it is expected in terms of work. Here, the outlet flow angle is defined with respect to the $x - axis$ of the absolute plane of reference and corresponds to β_2 in Fig. 37.

Figure 37: Side representation of the blade in absolute axis, with inflow and outflow represented respectively in blue and red.

Outflow angle is computed from time-averaged velocity fields, which are in Appendix D. The velocities are extracted at the same place where the losses in the Section 4.4 have been calculated. The time-averaged outlet flow angle is then computed as

$$\overline{\beta_2}(y) = \arctan \frac{\overline{v_y}}{\overline{v_x}}. \tag{16}$$

The mean time-averaged outlet flow angle is computed by integration of Eq. 16 over the height of the domain, as

$$\beta_2 = \frac{\int \overline{\beta_2}(y) dy}{\int dy}. \tag{17}$$

Results from Eq. 17, on the measurement plane half a chord after the TE, are shown in the Tab. 5.

Solidity σ [-]	**Incidence [°]**	**Flow angle [°]**
1.1	6	9.9697
	8	11.4409
1.38	6	7.9655
	8	8.0642

Table 5: Integrated time-averaged outlet flow angles β_2.

Comparison of integrated time-averaged outflow angle of experimental data and DNS data is shown in Fig. 38. A linear curve fitting of experimental data is made using a least-squares method. In the case of the low solidity shown in Fig. 38a, the DNS results show a difference of -2.35% and -1.12% respectively for 6 and 8° incidences. Overall, the outflow angles computed numerically are very close to the ones observed experimentally.

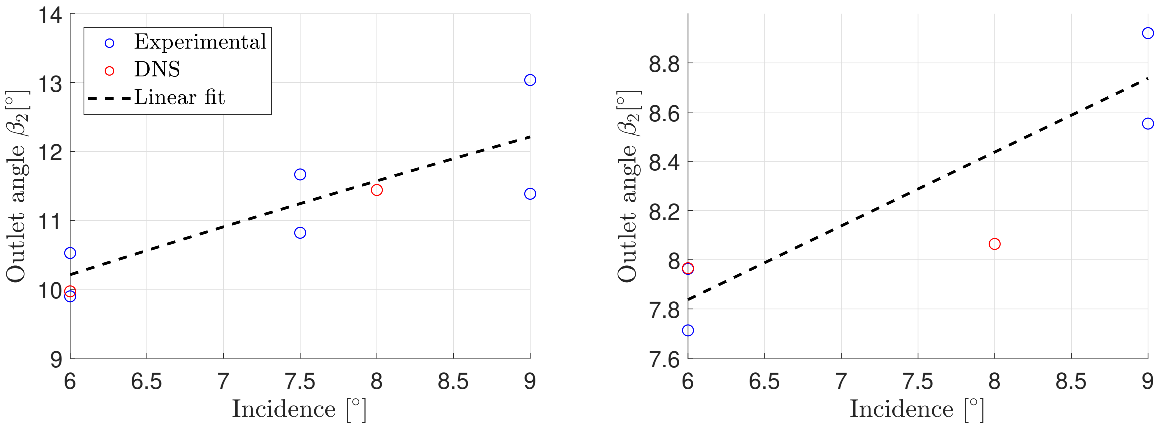

(a) Solidity $\sigma = 1.1$ (b) Solidity $\sigma = 1.38$

Figure 38: Comparison of integrated time-averaged outflow angle of experimental data and DNS data.

The same approach is used for the configuration at higher solidity, results are shown in Fig. 38b. Computed outflow angles do not match as well as for lower solidity. Numerical angles show a difference of 1.5% and -4.6379% respectively for 6° and 8° incidences. For the case at 6° incidence, the same explanation as in the previous section can be made. Since there are fewer losses, the flow deviation is greater. Although the losses in the system were greatly undervalued, the difference in angles is not so pronounced. For the case at 8° of incidence, the flow angle is underestimated. The calculated losses being overestimated, it is normal to observe a deviation of the flow which is weaker. This same observation can be seen in the experimental data which are available in the Appendix F.

4.6 Computational time and cost

DNS are much more expensive compared to RANS. A mesh partition of more or less 1000 elements requires around 1.5 GB of ram. It is caused by the fact that for one quad elements, there are 64 associated degrees of freedom.

In a general manner, the storage is a real problem in such computation. Saving intermediate solution can reach up to 3.5 GB per save. And exporting different data on different surfaces/volumes can rapidly lead to a hundred thousand of files for few hours of computation.

The most expensive operation for the LES is the computation of Jacobian. This operation takes in averages between 30 and 40 seconds. To save a lot of computational time, the Jacobian is reevaluated every 5 time step. To put this into perspective, for a computation using 224 CPU 10 hours of computation can reach between 1000 and 1200 iterations. Tab. 6 summarized the number of elements, the number of degrees of freedom, the averaged time it takes to compute jacobian and the CPU hours for every simulation.

Solidity σ	**Incidence [$^\circ$]**	**Mesh elements**	**Degrees of freedom**	**Jacobian comp. time [s]**	**CPU Hours**
1.1	6	293 004	18 642 528	40	33 600
	8			30	126 336
1.38	6	314 244	19 935 360	30	35 840
	8			34	31360
				Total	227 136

Table 6: Synthesis of the various characteristic parameters of each computation, which makes it possible to highlight the cost of the method of calculation.

5 Conclusions

This paper presented the results obtained using Direct Navier-Stokes (DNS) simulations on a low compressor blade at low Reynolds number. It aimed to highlight the differences in flow physics under different flow conditions.

In a first part, particular attention has been paid to presenting the methodology for setting up the simulations. Mesh resolution was sufficiently fine enough to guarantee the correct representation of small turbulent structures. Velocity correlations have shown that a span extrusion of 5% of the chord is sufficient only to ensure that the periodic walls do not influence the flow.

In general, the flow field is characterized by an extremely thick boundary layer on the suction side and a laminar flow on the pressure side. For the high incidence flow, the boundary layer reaches a thickness of 10% of the chord. All the flow conditions are subjected to Laminar separation bubble and turbulent flow reattachment near the leading edge. At high incidence and low solidity, the laminar separation bubble is very thick and short. Visualizations of the flow field revealed a flow separation that occurs 60% of the chord.

Moreover, for the high incidence and low solidity flow, there is a very small supersonic pocket present at the leading-edge. This small supersonic pocket is responsible for flow local flow acceleration. This causes the laminar separation to occur earlier, resulting in a thick laminar bubble, causing the boundary layer to be very thick.

The losses in the cascade were computed using the total pressure weighted by the mass flux. Results were compared to experimental data, and they showed a great agreement. Losses were predicted with differences in the order of 10% between experimental and numerical results. The same comparison was done using the outlet flow angles, and the matching is just as good, with differences in the order of the few pour cents. This is due to the fact that DNS is able to correctly predict the separation of the flow. It this better estimates the shape and height of the boundary layer.

In a future work, it would be interesting to dive in a different method so that the turbulence sets in more quickly. Such as three-dimensional velocity perturbation. It would also be interesting to analyze the physics of the flow with a turbulence intensity which is not zero at the inlet. It would also be interesting to carry on the same computation using a domain that is extruded twice and three times the width of the actual domain. It would allow comparing the veracity of the analyses made with the velocity correlations.

References

[1] Clusters at céci, https://www.ceci-hpc.be/clusters.htmlnic5.

[2] Sabah Alhamdi and Dr Taie. Flow separation of axial compressor cascade blades. *The Journal of Engineering*, 16:4877 – 4896, 06 2010.

[3] Hester Bijl, Mark H. Carpenter, Veer N. Vatsa, and Christopher A. Kennedy. Implicit time integration schemes for the unsteady compressible navier–stokes equations: Laminar flow. *Journal of Computational Physics*, 179(1):313–329, 2002.

[4] Jean-Sébastien Cagnone, Michel Rasquin, Koen Hillewaert, and Stéphane Hiernaux. Large eddy simulation of a low pressure compressor cascade at high incidence. 01 2017.

[5] Corentin Carton de Wiart, Ariane Frère, and Koen Hillewaert. Towards wall-modelled implicit les with a discontinuous galerkin method. 09 2014.

[6] Corentin Carton de Wiart, Koen Hillewaert, and Philippe Geuzaine. Dns of a low pressure turbine blade computed with the discontinuous galerkin method. volume 8, 06 2012.

[7] Koen Hillewaert. *Development of the discontinuous Galerkin method for high-resolution, large scale CFD and acoustics in industrial geometries*. PhD thesis, 02 2013.

[8] Koen Hillewaert. *Flow in turbomachines*, volume 1. University of Liège, 2021.

Appendices

A Time-averaged s^+ and n^+ on the blade

A.1 n^+

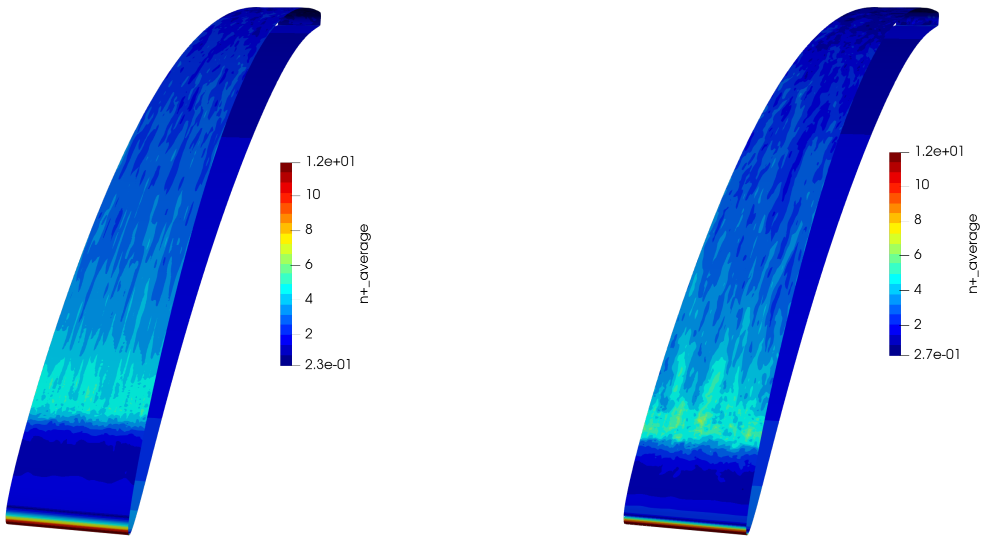

(a) Solidity σ = 1.1 and incidence i = 6°

(b) Solidity σ = 1.1 and incidence i = 8°

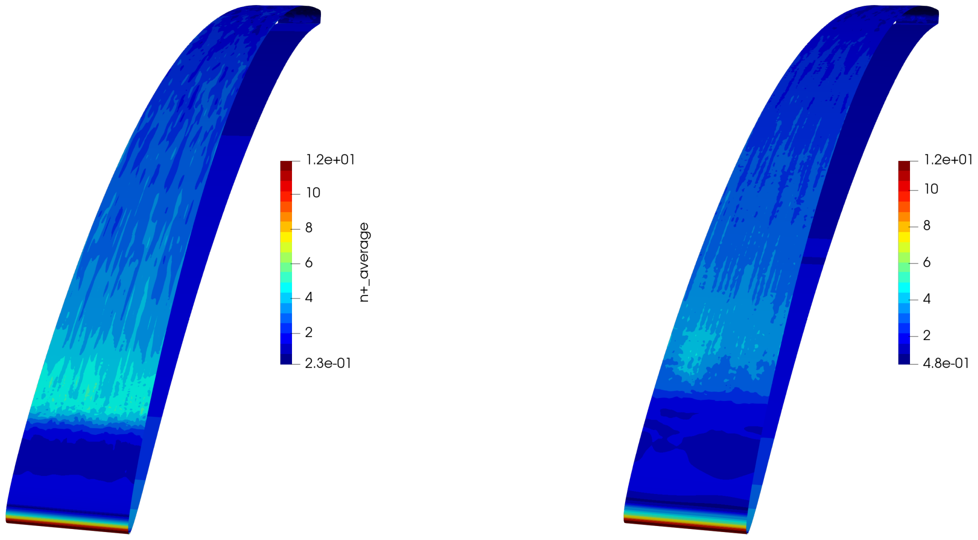

(c) Solidity σ = 1.38 and incidence i = 6°

(d) Solidity σ = 1.38 and incidence i = 8°

Figure 39: Time-averaged n^+ contours field over the blade surface for each flow conditions.

A.2 s^+

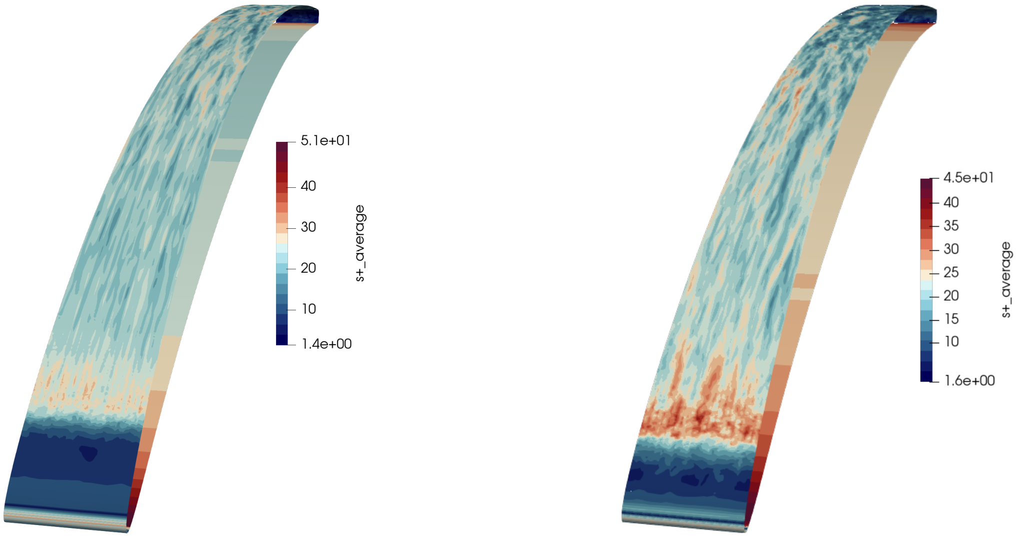

(a) Solidity σ = 1.1 and incidence i = 6° (b) Solidity σ = 1.1 and incidence i = 8°

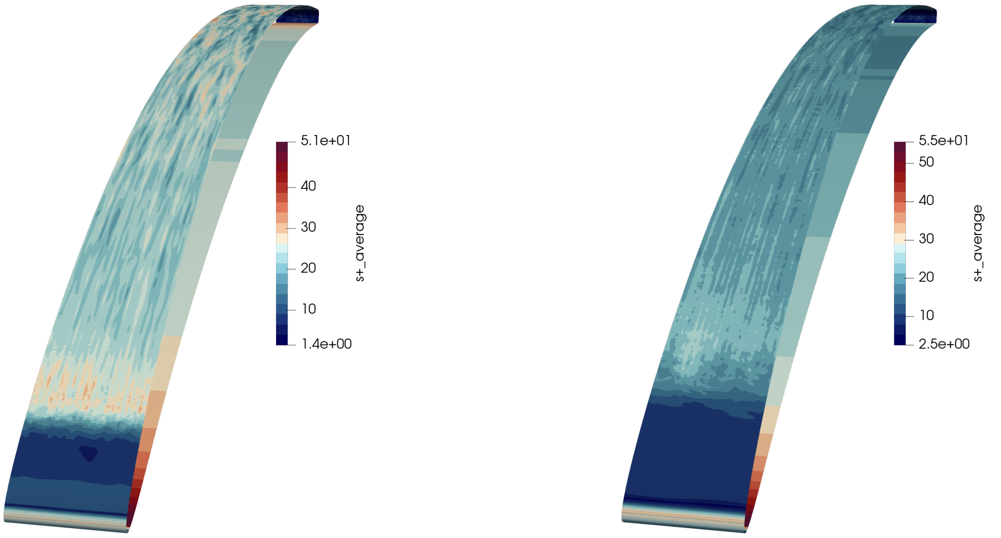

(c) Solidity σ = 1.38 and incidence i = 6° (d) Solidity σ = 1.38 and incidence i = 8°

Figure 40: Time-averaged n^+ contours field over the blade surface for each flow conditions.

B Overview of the general flow behavior inside the cascade

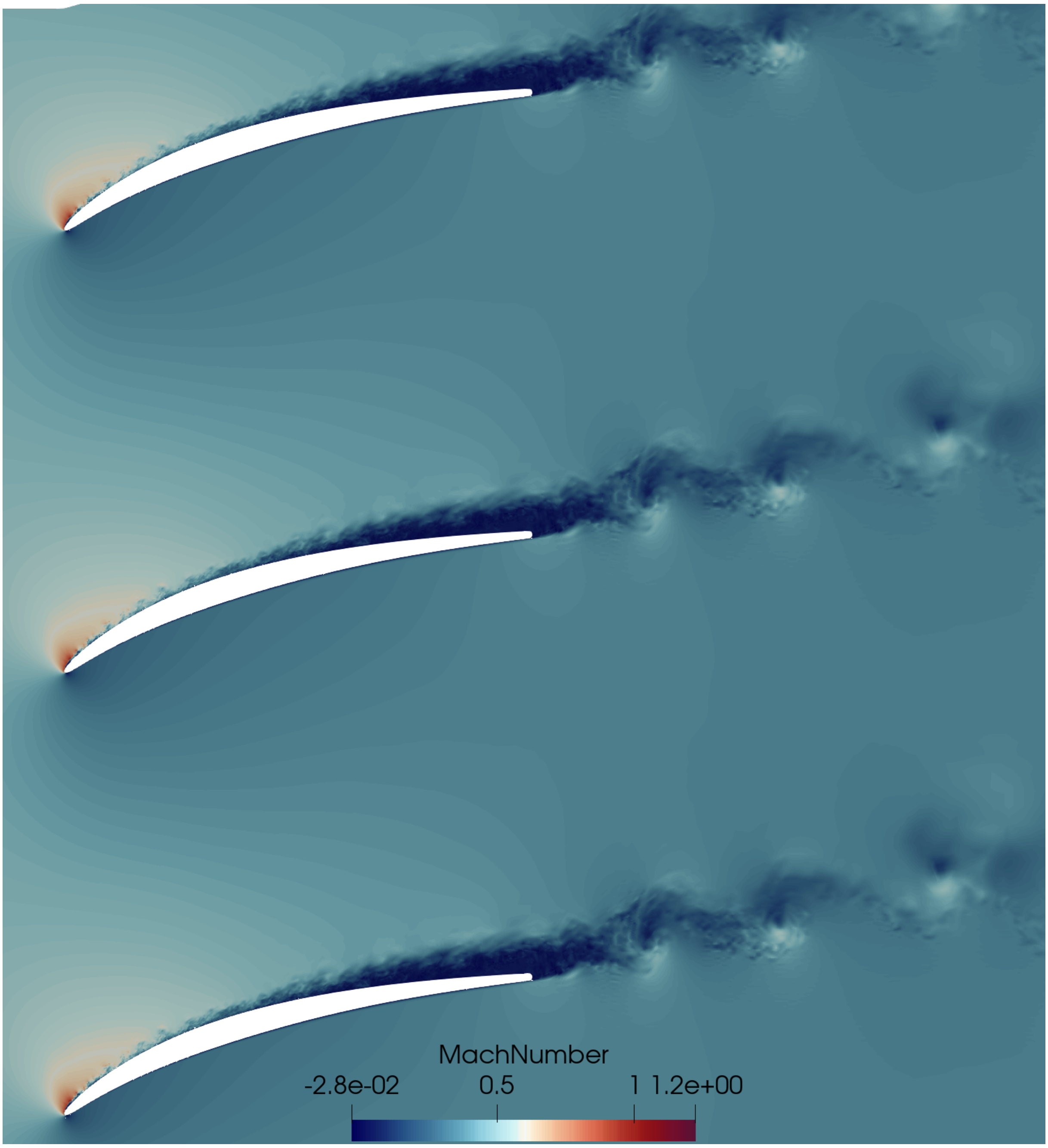

Figure 41: Instantaneous Mach number inside the blade cascade at an incidence $i = 8°$ and a solidity σ = 1.1.

C Time-averaged skin friction fields

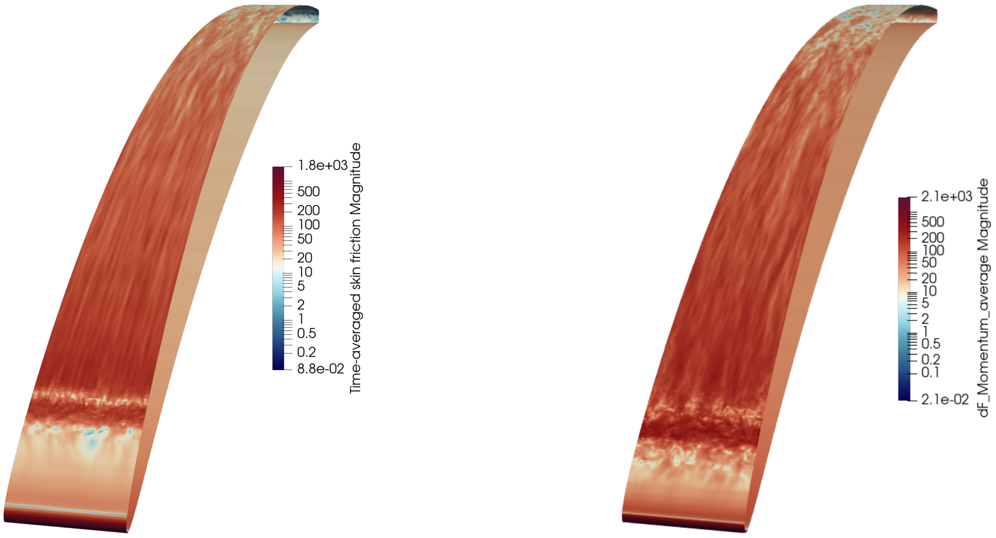

(a) Solidity σ = 1.1 and incidence i = 6°

(b) Solidity σ = 1.1 and incidence i = 8°

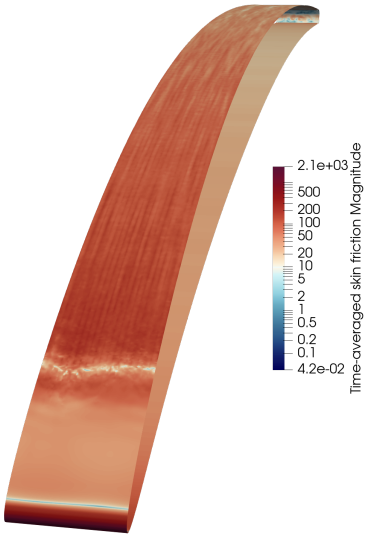

(c) Solidity σ = 1.38 and incidence i = 8°

Figure 42: Time-averaged skin friction, in logarithmic scale, over the blade surface for each flow conditions.

D Time-averaged velocity fields

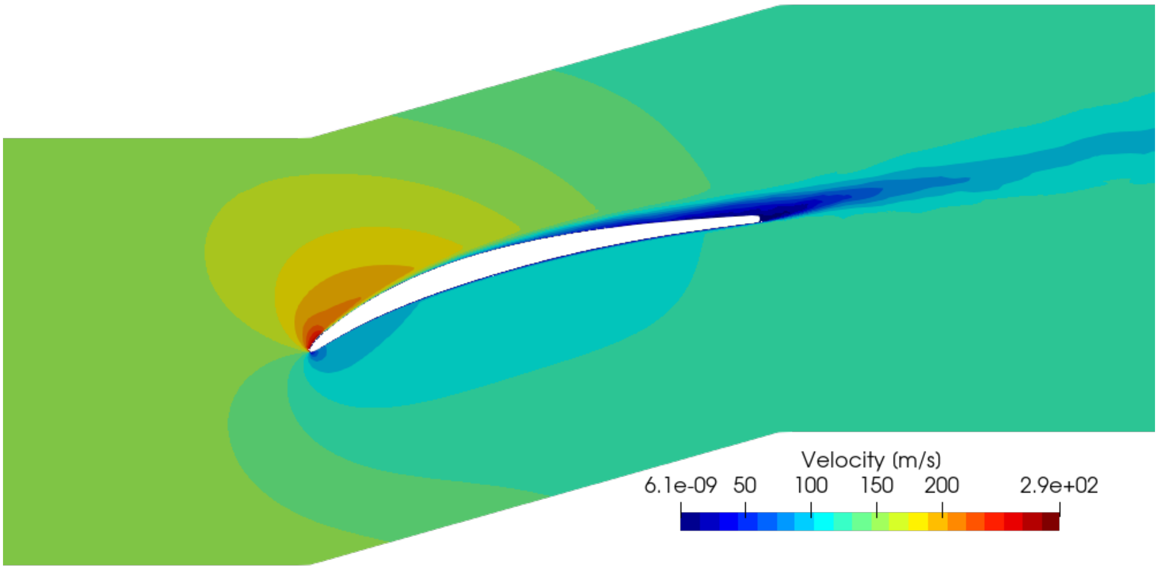

Figure 43: Time-averaged velocity field [m/s] at $i = 6°$ and solidity $\sigma = 1.1$. Contours are shown with 20 subdivisions.

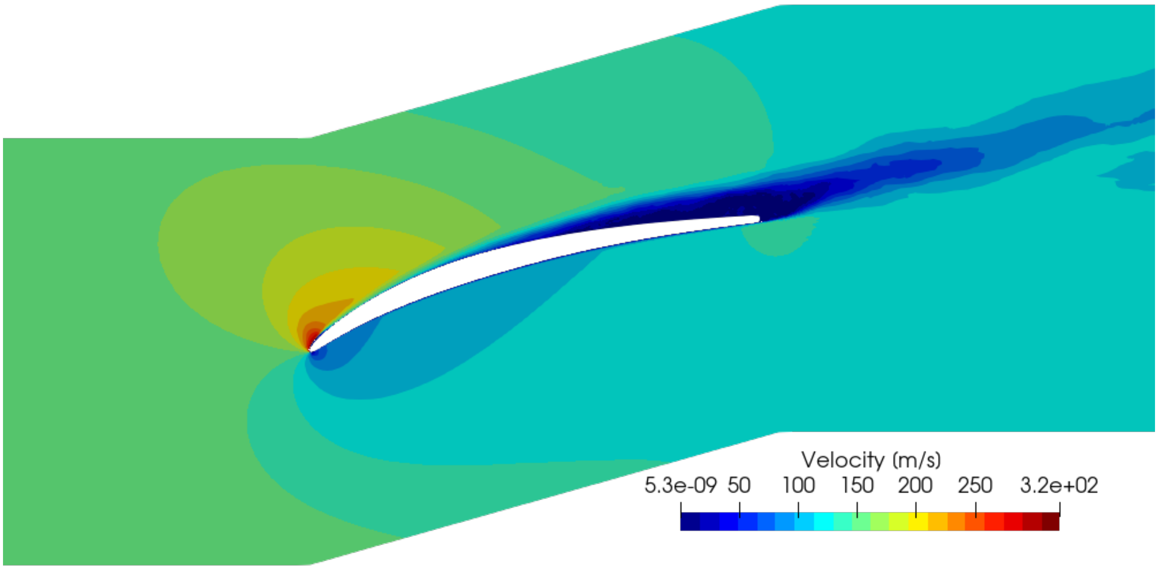

Figure 44: Time-averaged velocity field [m/s] at $i = 8°$ and solidity $\sigma = 1.1$. Contours are shown with 20 subdivisions.

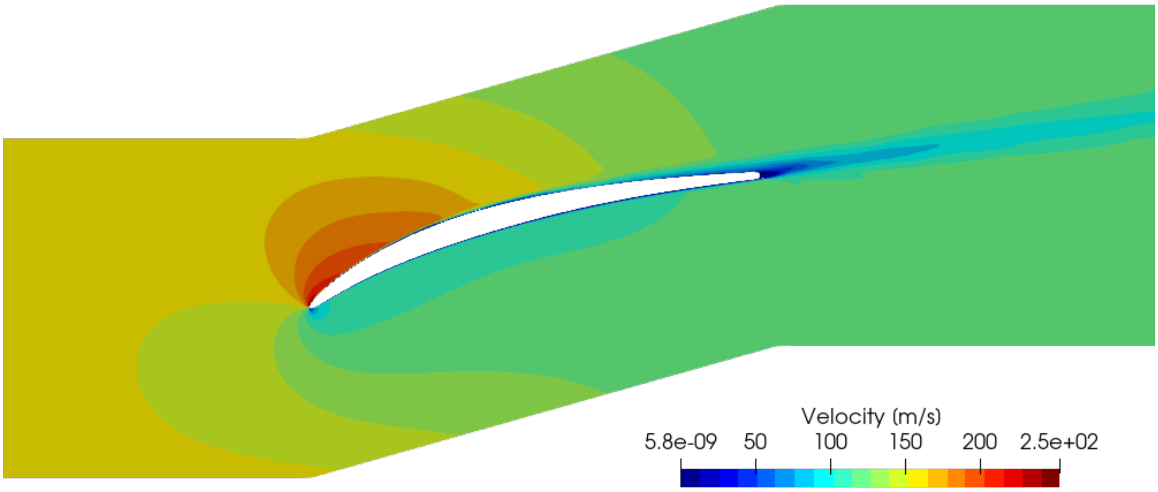

Figure 45: Time-averaged velocity field [m/s] at $i = 6^{\circ}$ and solidity $\sigma = 1.38$. Contours are shown with 20 subdivisions.

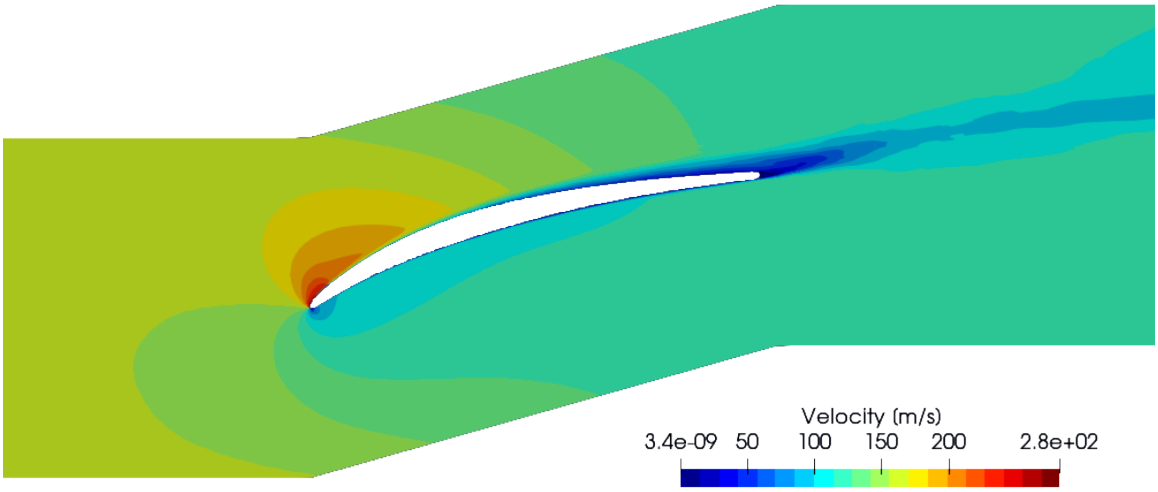

Figure 46: Time-averaged velocity field [m/s] at $i = 8^{\circ}$ and solidity $\sigma = 1.38$. Contours are shown with 20 subdivisions.

E Time-averaged total pressure fields

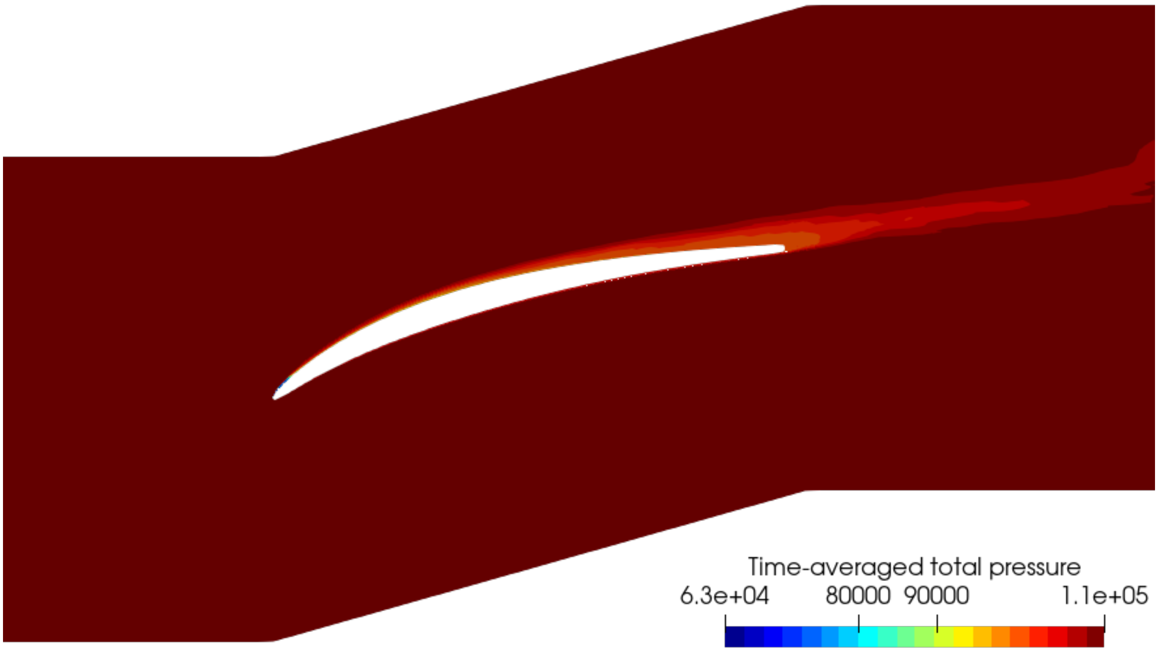

Figure 47: Time-averaged total pressure [Pa] at $i = 6°$ and solidity $\sigma = 1.1$. Contours are shown with 20 subdivisions.

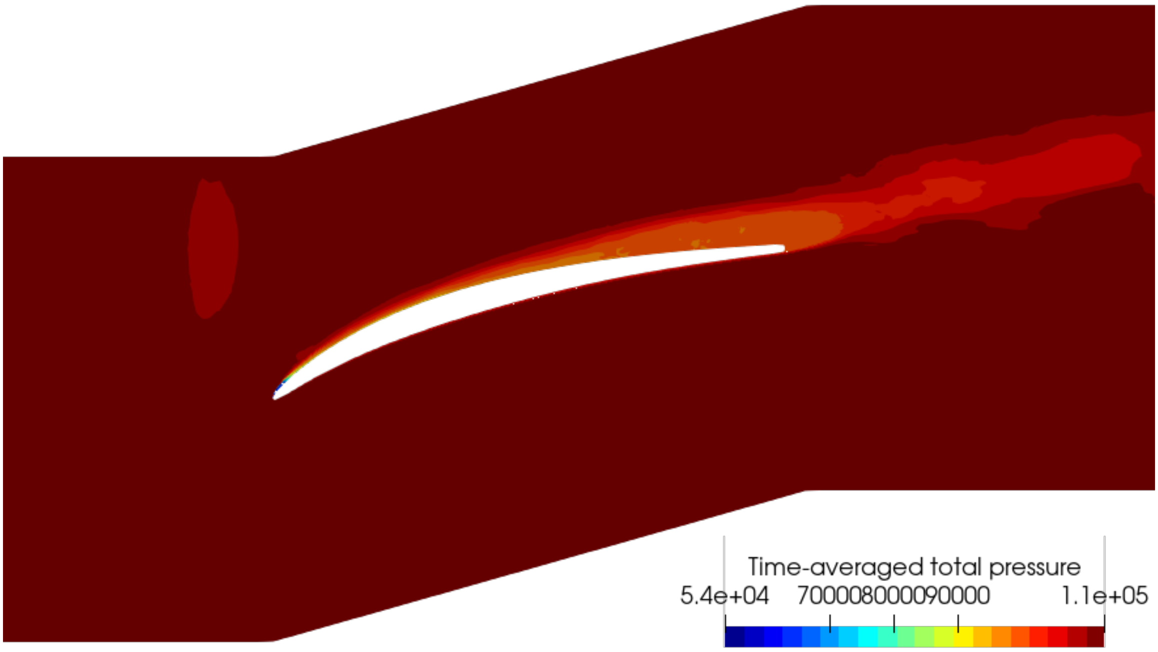

Figure 48: Time-averaged total pressure [Pa] at $i = 8°$ and solidity $\sigma = 1.1$. Contours are shown with 20 subdivisions.

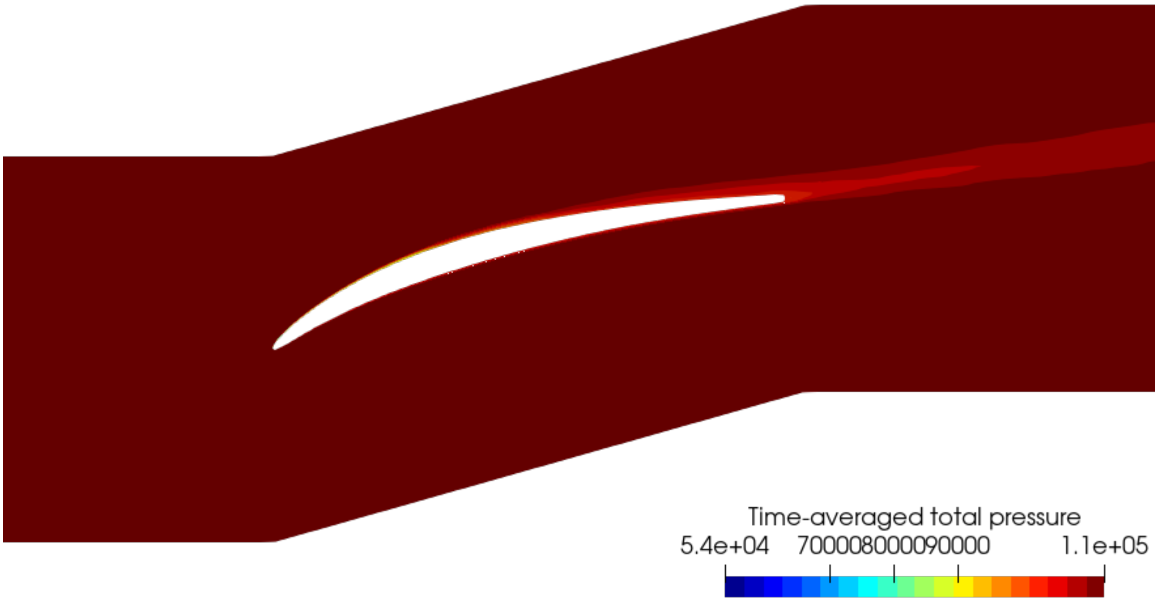

Figure 49: Time-averaged total pressure [Pa] at $i = 6°$ and solidity $\sigma = 1.38$. Contours are shown with 20 subdivisions.

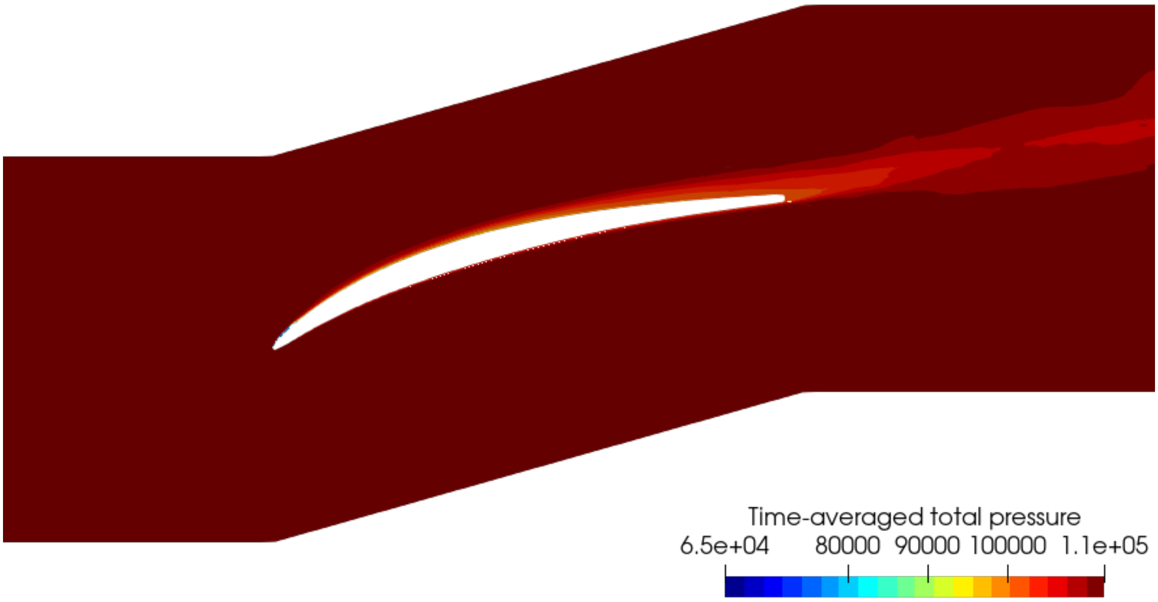

Figure 50: Time-averaged total pressure [Pa] at $i = 8°$ and solidity $\sigma = 1.38$. Contours are shown with 20 subdivisions.

F Experimental results carried by Safran Aero Boosters

		Experiment 1	
Solidity σ [-]	**Incidence [°]**	**Loss Coefficient [-]**	**Outlet flow angle β_2 [°]**
1.1	6	0,02698134081	10,52609146
	7.5	0,04637824822	11,66652827
	9	0,1531078	13,03719784
1.38	6	0,0166027061	7,963007091
	9	0,02900586318	8,921020193
		Experiment 2	
Solidity σ [-]	**Incidence [°]**	**Loss Coefficient [-]**	**Outlet flow angle β_2 [°]**
1.1	6	0,02697092184	9,897078811
	7.5	0,04958277101	10,81990832
	9	0,213692359	11,38603605
1.38	6	0,0178008866	7,712780293
	9	0,03243529511	8,553337726

Table 7: Experimental results carried by Safran Aero Boosters on a cascade test bench for two incidences at two solidities for a Mach number of $M = 0.45$.

G Time-averaged static pressure field

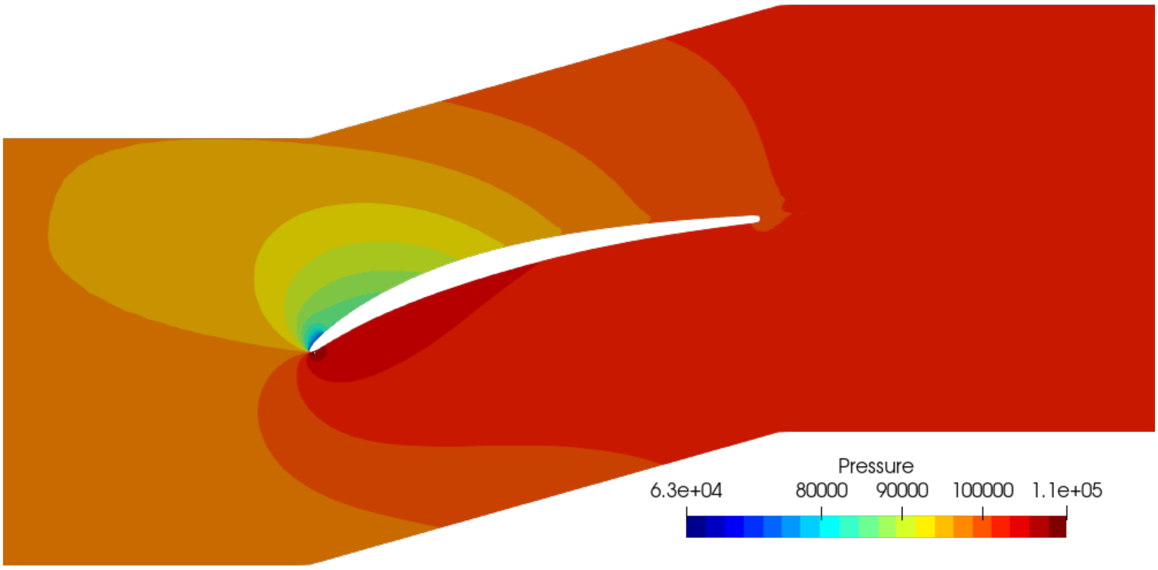

Figure 51: Time-averaged static pressure field at $i = 6°$ and solidity $\sigma = 1.1$. Contours are shown with 20 subdivisions.

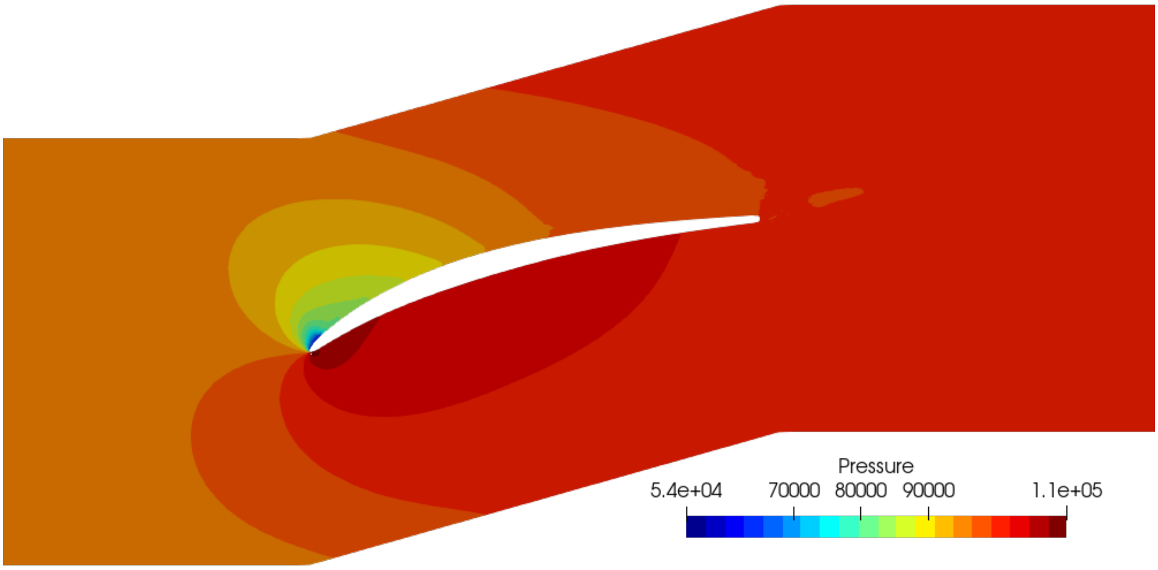

Figure 52: Time-averaged static pressure field at $i = 8°$ and solidity $\sigma = 1.1$. Contours are shown with 20 subdivisions.

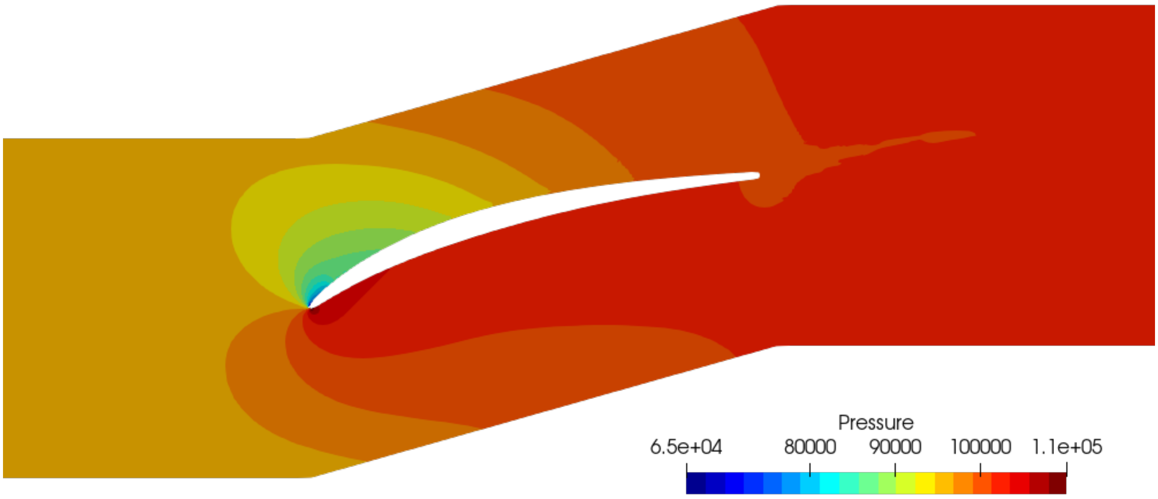

Figure 53: Time-averaged static pressure field at $i = 8°$ and solidity $\sigma = 1.38$. Contours are shown with 20 subdivisions.

H Time-averaged isentropic Mach number field

H.1 Full domain

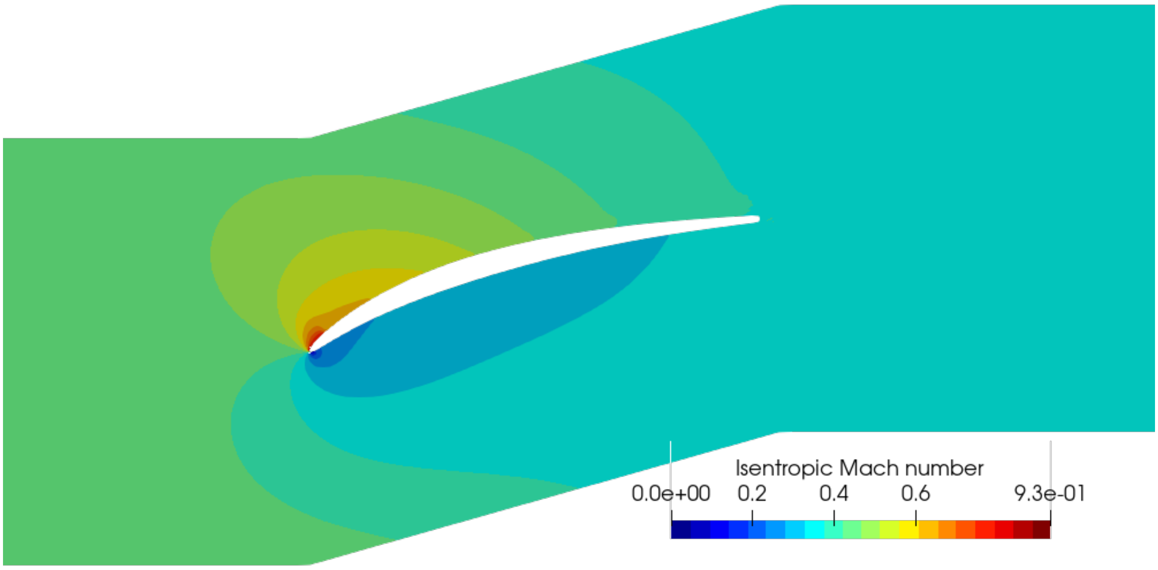

Figure 54: Time-averaged isentropic Mach number at $i = 6°$ and solidity $\sigma = 1.1$. Contours are shown with 20 subdivisions.

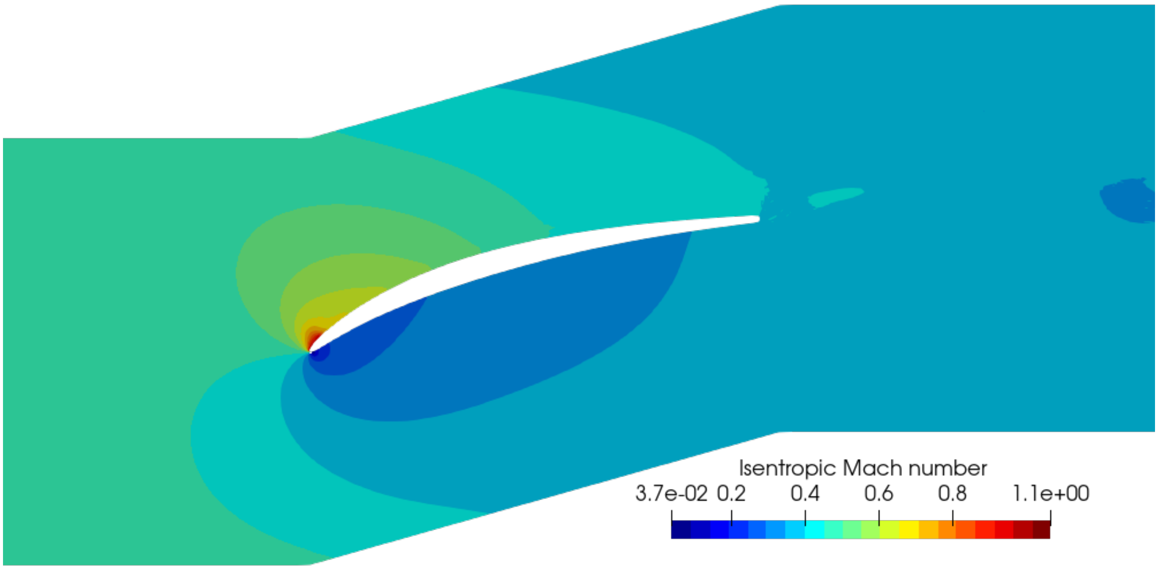

Figure 55: Time-averaged isentropic Mach number at $i = 8°$ and solidity $\sigma = 1.1$. Contours are shown with 20 subdivisions.

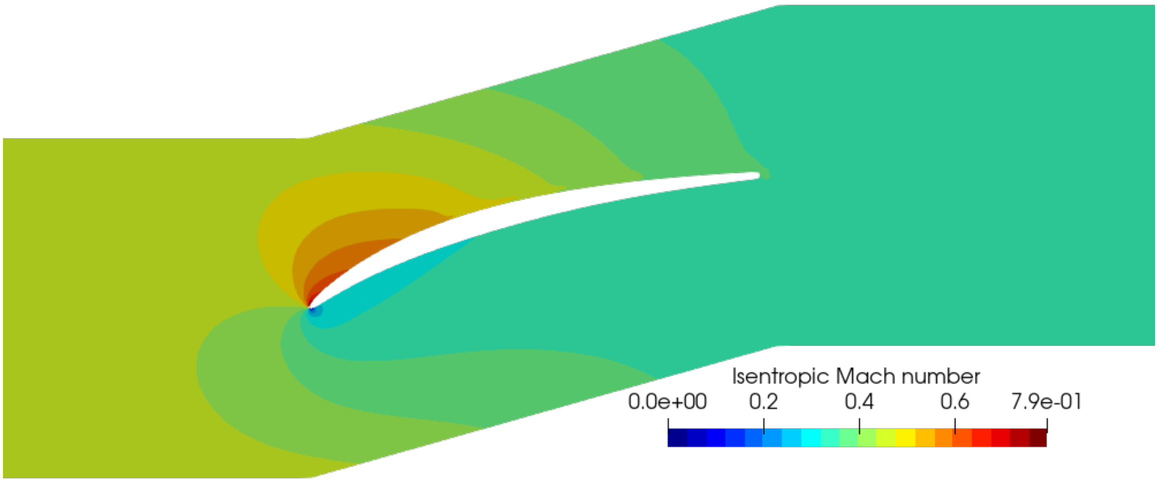

Figure 56: Time-averaged isentropic Mach number at $i = 6°$ and solidity $\sigma = 1.38$. Contours are shown with 20 subdivisions.

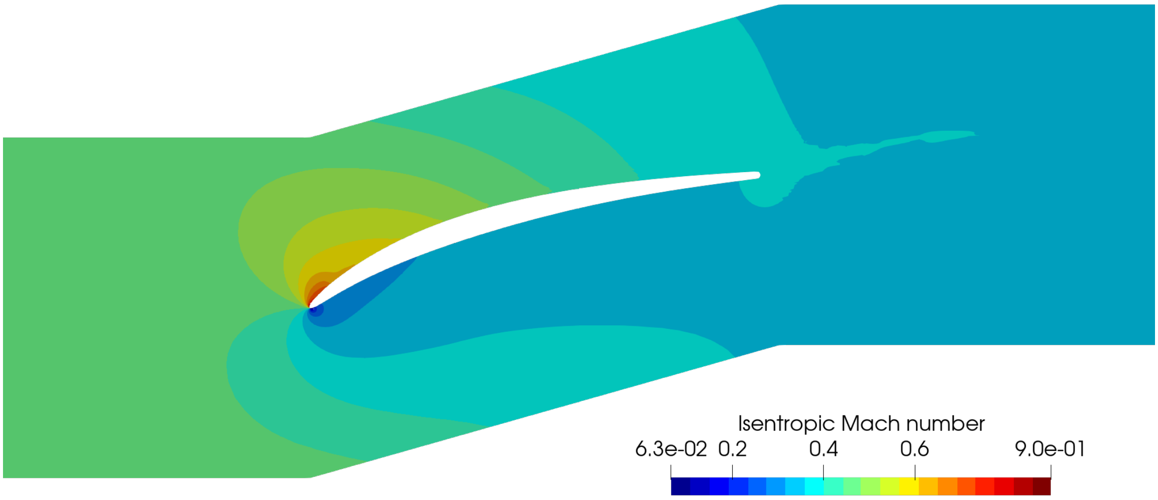

Figure 57: Time-averaged isentropic Mach number at $i = 8°$ and solidity $\sigma = 1.38$. Contours are shown with 20 subdivisions.

H.2 Zoom on the leading-edge

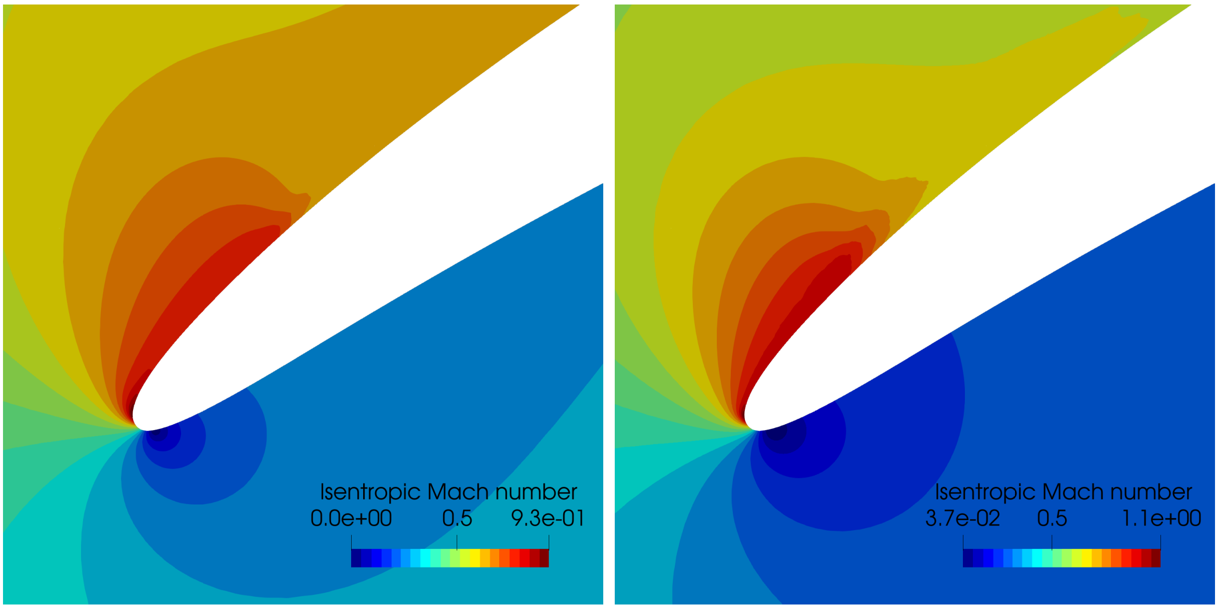

(a) $i = 6°$ and $M_{is,max} = 0.93$

(b) $i = 8°$ and $M_{is,max} = 1.05$

Figure 58: Zoom on the leading-edge of the isentropic Mach number. The blade solidity is $\sigma = 1.1$ for both flow incidences.

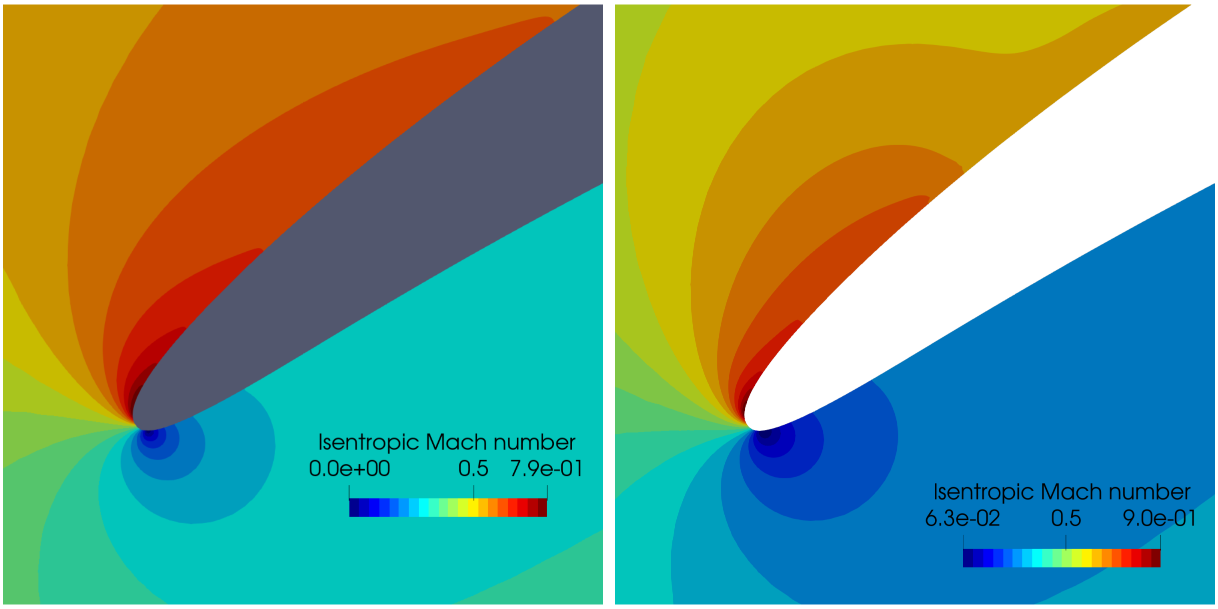

(a) $i = 6°$

(b) $i = 8°$

Figure 59: Zoom on the leading-edge of the isentropic Mach number. The blade solidity is $\sigma = 1.38$ for both flow incidences.